



AFRL-OSR-VA-TR-2013-0613

**VIBRATION SUPPRESSION STRATEGIES FOR LARGE
TENSION-ALIGNED ARRAY STRUCTURES**

RANJAN MUKHERJEE

MICHIGAN STATE UNIVERSITY

**11/19/2013
Final Report**

DISTRIBUTION A: Distribution approved for public release.

**AIR FORCE RESEARCH LABORATORY
AF OFFICE OF SCIENTIFIC RESEARCH (AFOSR)/RSA
ARLINGTON, VIRGINIA 22203
AIR FORCE MATERIEL COMMAND**

REPORT DOCUMENTATION PAGE				Form Approved OMB No. 0704-0188	
Public reporting burden for this collection of information is estimated to average 1 hour per response, including the time for reviewing instructions, searching existing data sources, gathering and maintaining the data needed, and completing and reviewing this collection of information. Send comments regarding this burden estimate or any other aspect of this collection of information, including suggestions for reducing this burden to Department of Defense, Washington Headquarters Services, Directorate for Information Operations and Reports (0704-0188), 1215 Jefferson Davis Highway, Suite 1204, Arlington, VA 22202-4302. Respondents should be aware that notwithstanding any other provision of law, no person shall be subject to any penalty for failing to comply with a collection of information if it does not display a currently valid OMB control number. PLEASE DO NOT RETURN YOUR FORM TO THE ABOVE ADDRESS.					
1. REPORT DATE (DD-MM-YYYY) 11-18-2013		2. REPORT TYPE Final Report		3. DATES COVERED (From - To) Sep 1, 2010 to Aug 31, 2013	
4. TITLE AND SUBTITLE Vibration Suppression Strategies for Large Tension-Aligned Array Structures				5a. CONTRACT NUMBER FA9550-10-1-0500	
				5b. GRANT NUMBER	
				5c. PROGRAM ELEMENT NUMBER	
6. AUTHOR(S) Ranjan Mukherjee Alejandro R. Diaz				5d. PROJECT NUMBER	
				5e. TASK NUMBER	
				5f. WORK UNIT NUMBER	
7. PERFORMING ORGANIZATION NAME(S) AND ADDRESS(ES) Michigan State University Department of Mechanical Engineering 428 S. Shaw Lane, Room 2555 East Lansing, MI 48824				8. PERFORMING ORGANIZATION REPORT NUMBER	
9. SPONSORING / MONITORING AGENCY NAME(S) AND ADDRESS(ES)				10. SPONSOR/MONITOR'S ACRONYM(S)	
				11. SPONSOR/MONITOR'S REPORT NUMBER(S)	
12. DISTRIBUTION / AVAILABILITY STATEMENT					
13. SUPPLEMENTARY NOTES					
14. ABSTRACT Tension-aligned structures have been proposed for space-based antenna applications. The structure uses a compression member to impart tension on the antenna, thus helping to maintain shape and facilitate disturbance rejection. These structures can be large and are therefore sensitive to low-frequency excitation. Three energy-based control strategies have been proposed for vibration suppression. The first strategy uses stiffness variation to funnel vibration energy from low-frequency modes to high-frequency modes of the structure, where it is dissipated naturally due to internal damping. The second control strategy uses a sliding mechanism to apply a moving constraint; the constraint force is measured in real time and is used to prescribe the motion of the slider. Energy of the structure is reduced continuously by doing negative work from the slider. The third strategy models the antenna as a thin plate and controls the tension on the boundary of the plate to suppress vibration. The Rayleigh-Ritz method was used to model the plate structure and an observer was used to estimate the modal amplitudes. For the second and third strategies, Lyapunov stability theory was used to show vibration suppression. Practical issues related to actuator bandwidth were also addressed.					
15. SUBJECT TERMS					
16. SECURITY CLASSIFICATION OF:			17. LIMITATION OF ABSTRACT	18. NUMBER OF PAGES 40	19a. NAME OF RESPONSIBLE PERSON Dr. Ranjan Mukherjee
a. REPORT	b. ABSTRACT	c. THIS PAGE			19b. TELEPHONE NUMBER (include area code) (517) 355-1834

FINAL PERFORMANCE REPORT

Vibration Suppression Strategies for Large Tension-Aligned Array Structures

AFOSR Grant FA9550-10-1-0500

Grant Period: September 1, 2010 to August 31, 2013

Ranjan Mukherjee Alejandro R. Diaz

Department of Mechanical Engineering
2555 Engineering Building
Michigan State University
East Lansing, MI 48824-1226

Email: {mukherji, diaz}@egr.msu.edu

Abstract

Tension-aligned structures have been proposed for space-based antenna applications. The structure uses a compression member to impart tension on the antenna, thus helping to maintain shape and facilitate disturbance rejection. These structures can be large and are therefore sensitive to low-frequency excitation. Three energy-based control strategies have been proposed for vibration suppression. The first strategy uses stiffness variation to funnel vibration energy from low-frequency modes to high-frequency modes of the structure, where it is dissipated naturally due to internal damping. The second control strategy uses a sliding mechanism to apply a moving constraint; the constraint force is measured in real time and is used to prescribe the motion of the slider. Energy of the structure is reduced continuously by doing negative work from the slider. The third strategy models the antenna as a thin plate and controls the tension on the boundary of the plate to suppress vibration. The Rayleigh-Ritz method was used to model the plate structure and an observer was used to estimate the modal amplitudes. For the second and third strategies, Lyapunov stability theory was used to show vibration suppression. Practical issues related to actuator bandwidth were also addressed.

Publications

Journal Papers:

- Alsahlani, A. and Mukherjee, R., “Vibration Control of a String Using a Scabbard-Like Actuator”, *Journal of Sound and Vibration*, **330**(2), pp. 2721-2732, 2011
- Alsahlani, A., Mathis, F. B., and Mukherjee, R., “Vibration Suppression of a String Through Cyclic Application and Removal of Constraints”, *Journal of Sound and Vibration*, **331**(20), pp. 4395-4405, 2012
- Alsahlani, A. and Mukherjee, R., “Dynamics of a Circular Membrane with an Eccentric Circular Areal Constraint: Analysis and Accurate Simulations”, *Simulation Modeling Practice and Theory*, **31**, pp. 149-168, Feb 2013
- Cai, T., Mukherjee, R., and Diaz, R., “Vibration Suppression in a Simple Tension-Aligned Array Structure”, *AIAA Journal*, DOI: 10.2514/1.J052127

Conference Papers:

- Alsahlani, A. and Mukherjee, R., “Dynamics Simulation of a Circular Membrane with an Eccentric Circular Areal Constraint”, *ASME International Design Engineering and Technical Conference (IDETC)*, Washington, DC, 2011
- Alsahlani, A. and Mukherjee, R., “Energetics of Circular Membrane Subjected to Eccentric Circular Areal Constraint”, *ASME International Design Engineering and Technical Conference (IDETC)*, Chicago, IL, 2012
- Alsahlani, A., Mathis, F. B., and Mukherjee, R., “Vibration Control of a String Using a Zero Displacement Constraint at a Point near One Boundary: Theory and Experiments”, *ASME International Design Engineering and Technical Conference (IDETC)*, Chicago, IL, 2012
- Cai, T., Mukherjee, R., and Diaz, R., “Vibration Suppression in a Tension Aligned Structure Through Sequential Application and Removal of Constraints”, *ASME International Design Engineering and Technical Conference (IDETC)*, Chicago, IL, 2012
- Cai, T., Mukherjee, R., and Diaz, R., “Vibration Suppression in a Pinned-Pinned Nonlinear Rod Using a Frictionless Slider”, *ASME International Design Engineering and Technical Conference (IDETC)*, Chicago, IL, 2012

1 Introduction

Large space structures have been contemplated for use as space-based radars for imaging and moving object identification and tracking. These radars will consist of a large support structure and phased array antennas attached to this structure. A high degree of accuracy is required but it is difficult to achieve since these structures are large and sensitive to low-frequency disturbances. Vibration suppression in large space structures is a challenging problem and a practical solutions need to be developed.

To meet the precision requirements of space-based radars, tension-aligned structures have been proposed by Mikulas et al. [1], and Jones et al. [2]. In these structures, the antennas are attached to the support structure via tensioners at each end (see Fig.1); the support structure is used as a compression member to impart tension. The tension in the antenna helps maintain flatness, but more importantly, increases its stiffness which is necessary for disturbance rejection [3]. Tension also increases structural damping [5] which facilitates vibration suppression. The tension-aligned architecture is equally well-suited for radar designs where the antennas are an array of panels or are attached to a flexible membrane [6, 7, 8].

The mass of antennas need to be minimized to reduce the required tension [7] and to reduce the overall mass and complexity of the system. Therefore, in tension-aligned structures, the sensor arrays are transformed into two-dimensional structures. To seek a balance between mass efficiency and structural stability, minimum thickness of the arrays is necessary. In a recently proposed structural solution [7, 8], the antenna consists of a series of linked semi-rigid panels connected to a catenary cable network. The highly flexible and low damping nature of the tensioned structure demands sufficient control for suppression of vibration. To this end, we explored three different control strategies; these are described in the next three sections.

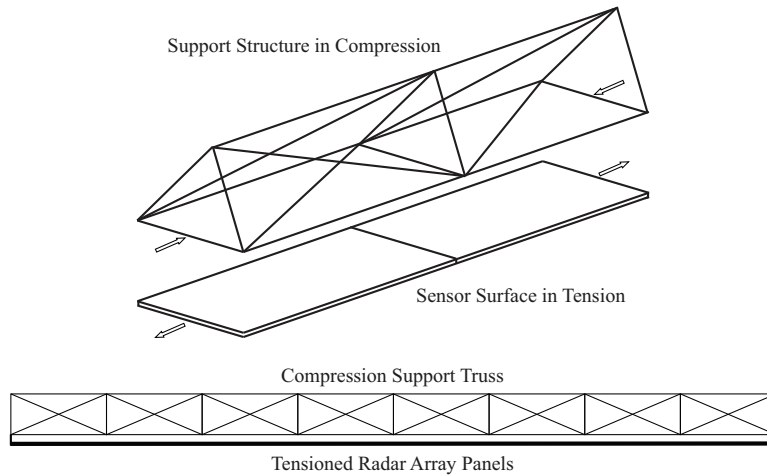


Figure 1: A tension-aligned structure comprised of a support structure and a sensor surface - taken from Jones et al. [2].

2 Vibration Suppression Through Stiffness Switching

In this section we discuss the first control strategy for vibration suppression. This strategy uses stiffness variation to funnel vibration energy from low-frequency modes to high-frequency modes of the structure, where it is dissipated naturally due to internal damping. The strategy is verified in simulations using both two-dimensional and three-dimensional models of tension aligned structures.

2.1 Stiffness Variation in Multi-DOF Systems

Consider the N -DOF linear system

$$\mathbb{M}\ddot{X} + \mathbb{K}(t)X = 0 \quad (1)$$

where $X = (x_1, x_2, \dots, x_N)^T$ denotes the vector of generalized coordinates, \mathbb{M} denotes the mass matrix, and $\mathbb{K}(t)$ denotes the stiffness matrix. The stiffness matrix $\mathbb{K}(t)$ consists of a constant stiffness matrix \mathbb{K}_0 and a time-varying stiffness matrix $\Delta\mathbb{K}(t)$ as follows

$$\mathbb{K}(t) = \mathbb{K}_0 + \Delta\mathbb{K}(t), \quad \Delta\mathbb{K}(t) = \begin{cases} 0 & \text{if } t \in [t_i, t_{i+1}) \\ K_r & \text{if } t \in [t_{i+1}, t_{i+2}) \end{cases}, \quad i = 0, 2, 4, \dots \quad (2)$$

where K_r is the change in the stiffness matrix due to the addition of springs connecting pairs of generalized coordinates. In the simplest case where a single spring is used to connect a pair of generalized coordinates x_m and x_n , the entries of $K_r \in R^{N \times N}$ can be obtained from the Hessian of the additional strain energy $(1/2)k_r(x_m - x_n)^2$:

$$K_r(i, j) = \begin{cases} k_r & \text{if } (i, j) = (m, m) \text{ or } (n, n) \\ -k_r & \text{if } (i, j) = (m, n) \text{ or } (n, m) \\ 0 & \text{otherwise} \end{cases} \quad m \neq n \quad (3)$$

where k_r is the stiffness of the spring, which is large compared to the magnitude of the entries of \mathbb{K}_0 .

In Eq.(2), t_j , $j = 0, 1, 2, \dots$, are chosen such that the change in stiffness does not increase the total energy of the system. This is assured by choosing the time t_j when switching $\Delta\mathbb{K}(t_j)$ from 0 to K_r (stiffness increase) such that all the relevant relative displacements are zero. In the simplest case mentioned above, where a single spring is used, t_j is chosen to switch $\Delta\mathbb{K}(t_j)$ from 0 to K_r (stiffness increase) such that $x_m(t_j) - x_n(t_j) = 0$. When $\Delta\mathbb{K}(t_j)$ is switched from K_r to 0 (stiffness decrease), t_j can be arbitrary. In this process of stiffness decrease, there might be direct and instantaneous loss of energy due to the fact that relative displacement is usually nonzero given arbitrary t_j . This direct energy loss only favorably reduces the energy of the system.

Let ϕ_i and μ_i , $i = 1, 2, \dots, N$, denote the linearly independent orthogonal mode shapes and the corresponding modal coordinates in the unconstrained state. Similarly, let ψ_i and ν_i , $i = 1, 2, \dots, N$, denote the linearly independent orthogonal mode shapes and the corresponding modal coordinates in the constrained state. At the time of application of the constraint ($\Delta\mathbb{K}$ changes from 0 to K_r), the generalized coordinates and their velocities can be expressed as follows

$$X(t_{i+1}) = \begin{cases} \sum_{i=1}^N \mu_i(t_{i+1}) \phi_i = \Phi \mu(t_{i+1}) \\ \sum_{i=1}^N \nu_i(t_{i+1}) \psi_i = \Psi \nu(t_{i+1}) \end{cases} \quad i = 0, 2, 4, \dots \quad (4)$$

$$\dot{X}(t_{i+1}) = \begin{cases} \sum_{i=1}^N \dot{\mu}_i(t_{i+1}) \phi_i = \Phi \dot{\mu}(t_{i+1}) \\ \sum_{i=1}^N \dot{\nu}_i(t_{i+1}) \psi_i = \Psi \dot{\nu}(t_{i+1}) \end{cases} \quad i = 0, 2, 4, \dots \quad (5)$$

where $\Phi = [\phi_1, \phi_2, \dots, \phi_N]$ and $\Psi = [\psi_1, \psi_2, \dots, \psi_N]$ are modal matrices in the unconstrained and constrained states, respectively. Using Eqs.(4) and (5), the transition of the system from the unconstrained state to the constrained state can be described by the relations

$$\nu(t_{i+1}) = \Gamma \mu(t_{i+1}), \quad \dot{\nu}(t_{i+1}) = \Gamma \dot{\mu}(t_{i+1}), \quad i = 0, 2, 4, \dots \quad (6)$$

where Γ is the modal disparity matrix [21, 22], and is given by the relation

$$\Gamma = \Psi^T \mathbb{M} \Phi \quad (7)$$

The transition of the system from the constrained state to the unconstrained state can be similarly described by the relations

$$\mu(t_i) = \Gamma^T \nu(t_i), \quad \dot{\mu}(t_i) = \Gamma^T \dot{\nu}(t_i), \quad i = 0, 2, 4, \dots \quad (8)$$

The transformation matrix Γ is the identity matrix when $K_r = 0$, *i.e.*, when no stiffness variation is introduced. When $K_r \neq 0$, $\Gamma(i, j) \neq 0$ for some values of i and j , $i \neq j$. This implies that energy will be transferred from the j -th mode of the unconstrained state to the i -th mode of the constrained state, and vice versa. If the frequency of the i -th mode of the constrained state is much higher than that of the j -th mode of the unconstrained state, the energy transferred from the low-frequency mode to the high-frequency mode will be quickly dissipated. This follows from the assumption of

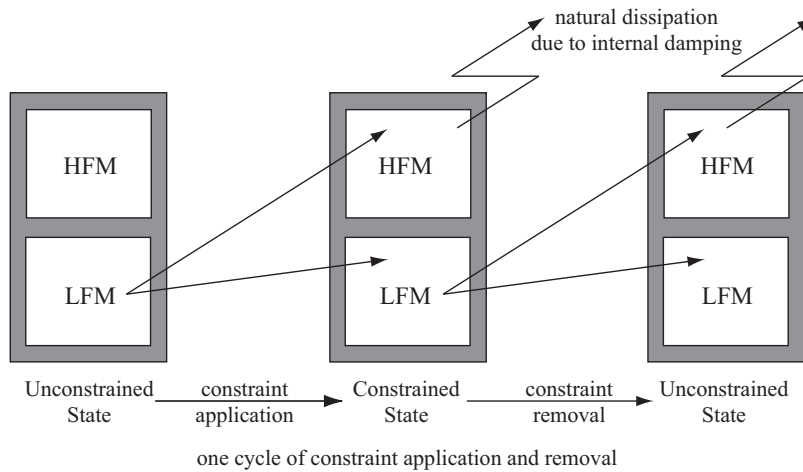


Figure 2: Vibration suppression through energy funneling from low-frequency modes (LFM) into high-frequency modes (HFM).

modal damping model with the uniform damping ratio. For the process to be repeated, the system has to be switched back from the constrained state to the unconstrained state. To avoid energy flow from the high-frequency modes in one state to the low-frequency modes in the other state, the system should be held in each state sufficiently long time such that energy in the high-frequency modes is dissipated. This strategy for vibration suppression is explained with the help of Fig.2.

The success of vibration suppression using stiffness switching depends on modal disparity created by the change in stiffness. To quantify modal disparity, a metric is defined

$$\lambda = \sum_{i=j+1}^N \sum_{j=1}^{N-1} (i-j) |\gamma_{ij}| \quad (9)$$

where $\gamma_{ij} = \Gamma(i, j)$ is the (i, j) -th entry of the modal disparity matrix Γ . This metric is a weighted sum of the projections of the low-frequency modes in the unconstrained state onto high-frequency modes in the constrained state and the weights are the difference of the indices of the modes in the two states. This metric was used to determine better location of constraints in a simple tension-aligned structure, modelled and simulated in the following subsections.

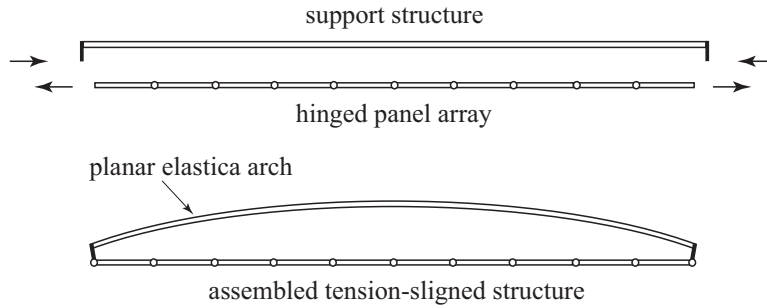


Figure 3: A tension-aligned structure constructed by connecting a support structure (in compression) to an array of hinged panels (in tension).

2.2 Model of a Two-Dimensional Simple Tension-Aligned Structure

In this subsection a finite-element model of a two-dimensional tension-aligned structure is presented. The tension-aligned structure, shown in Fig.3, consists of a planar elastica arch support structure in compression and a hinged panel array in tension. The planar elastica arch is initially a straight slender rod; it is bent into a curved shape by eccentric end loads that maintain equilibrium with the tension forces in the panels.

2.2.1 Nonlinear Dynamic Model of the Support Structure

The dynamic model of the elastica arch was reproduced from the work by Perkins [23]. The elastica arch, shown in Fig.4, is assumed to be a slender rod of length L , held in static equilibrium under the horizontal end-load f and moment fd , where d denotes the vertical eccentricity of the end-load f . In a disturbed state, a point on the rod has a displacement of $\vec{u}(s, t)$, where s denotes the

arc length along the centerline of the static equilibrium shape, and t denotes time. $\vec{u}(s, t)$ can be decomposed into its tangential component and normal components as follows

$$\vec{u}(s, t) = u_t(s, t) \hat{e}_t + u_n(s, t) \hat{e}_n$$

where \hat{e}_t and \hat{e}_n are unit vectors along the tangential and normal directions of the static equilibrium shape, shown in Fig.4.

Kirchhoff's assumptions for rod deformation [24] are taken, which are: (i) rod is linearly elastic, (ii) strains are small (although rotations may be large) and cross-sectional dimensions of the rod are small compared to its length, (iii) cross-sections remain plane, undistorted and normal to the axis of the rod, and (iv) the transverse stress and rotary inertia can be neglected. Under these assumptions, the kinetic energy and the strain energy of the rod can be expressed as follows

$$\Pi_T = \frac{1}{2} \int_0^L \rho \left[\left(\frac{\partial u_t}{\partial t} \right)^2 + \left(\frac{\partial u_n}{\partial t} \right)^2 \right] ds \quad (10)$$

$$\Pi_V = \frac{1}{2} \int_0^L (EI k^2 + EA e^2) ds \quad (11)$$

where ρ , E , A and I are constants and denote the mass per unit length, Young's modulus, cross-sectional area, and area moment of inertia of the rod, respectively. In Eq.(11) $k = k(s, t)$ and $e = e(s, t)$ are the curvature and the axial strain. The expression for $k(s, t)$ is obtained from Love [25] and that of $e(s, t)$ is obtained from Perkins and Mote [26]:

$$k = k_s + \frac{\partial}{\partial s} \left(\frac{\partial u_n}{\partial s} + k_s u_t \right) \quad (12)$$

$$e = \frac{p}{EA} = \frac{p_s}{EA} + \frac{\partial u_t}{\partial s} - k_s u_n + \frac{1}{2} \left[\left(\frac{\partial u_t}{\partial s} - k_s u_n \right)^2 + \left(\frac{\partial u_n}{\partial s} + k_s u_t \right)^2 \right] \quad (13)$$

where $p = p(s, t)$ is the axial force, and p_s and k_s are the static values of p and k , respectively, in the static equilibrium configuration.

The work done by external forces can be expressed as

$$W_{nc} = f (u_t \cos \theta_0 + u_n \sin \theta_0)|_{s=0} + f d \left(\frac{\partial u_n}{\partial s} + k_s u_t \right) \Big|_{s=0}^{s=L} \quad (14)$$

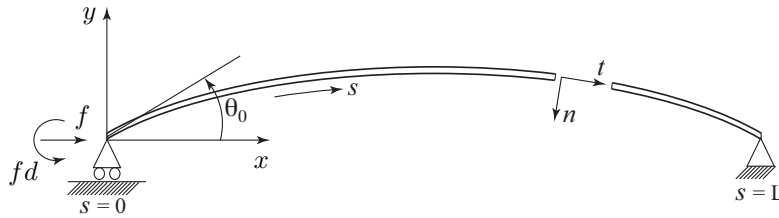


Figure 4: A planar elastica arch

where θ_0 is the angle of inclination of the rod at $s = 0$, which will be determined later. Substituting Eqs.(12) and (13) into Eq.(11); neglecting terms that have degree three and higher of variables u_t and u_n , and their spatial derivatives; and using Hamilton's principle

$$\delta \int_{t_1}^{t_2} (\Pi_T - \Pi_V + W_{nc}) dt = 0 \quad (15)$$

one gets the non-dimensional equations of motion in the normal and tangential directions [23]

$$\begin{aligned} -\frac{\partial^3}{\partial S^3} \left(\frac{\partial U_n}{\partial S} + KU_t \right) + \frac{\partial}{\partial S} \left[P \left(\frac{\partial U_n}{\partial S} + KU_t \right) \right] \\ + K \left(P + \frac{1}{\bar{I}} \right) \left(\frac{\partial U_t}{\partial S} - KU_n \right) - \frac{\partial^2 K}{\partial S^2} + PK = \frac{\partial^2 U_n}{\partial T^2} \end{aligned} \quad (16)$$

$$\begin{aligned} K \left[\frac{\partial^2}{\partial S^2} \left(\frac{\partial U_n}{\partial S} + KU_t \right) \right] + \frac{\partial}{\partial S} \left[\left(P + \frac{1}{\bar{I}} \right) \left(\frac{\partial U_t}{\partial S} - KU_n \right) \right] \\ - KP \left(\frac{\partial U_n}{\partial S} + KU_t \right) + K \frac{\partial K}{\partial S} + \frac{\partial P}{\partial S} = \frac{\partial^2 U_t}{\partial T^2} \end{aligned} \quad (17)$$

In the equations above, the non-dimensional variables are defined as follows

$$\begin{aligned} S \triangleq \frac{s}{L}, \quad D \triangleq \frac{d}{L}, \quad U_t \triangleq \frac{u_t}{L}, \quad U_n \triangleq \frac{u_n}{L}, \quad K \triangleq k_s L \\ P \triangleq \frac{p_s L^2}{EI}, \quad F \triangleq \frac{f L^2}{EI}, \quad \bar{I} \triangleq \frac{I}{AL^2}, \quad T \triangleq \frac{t}{(\rho L^4/EI)^{1/2}} \end{aligned} \quad (18)$$

Together with the equations of motion, the following boundary conditions are obtained from Hamilton's principle:

$$\begin{aligned} & \left\{ \left[\frac{\partial}{\partial S} \left(\frac{\partial U_n}{\partial S} + KU_t \right) + K - FD \right] \delta \left[\frac{\partial U_n}{\partial S} \right] \right\}_{S=0} \\ & + \left\{ \left[-\frac{\partial}{\partial S} \left[\frac{\partial}{\partial S} \left(\frac{\partial U_n}{\partial S} + KU_t \right) + K \right] + P \left(\frac{\partial U_n}{\partial S} + KU_t \right) + F \sin \theta_0 \right] \delta U_n \right\}_{S=0} \\ & + \left\{ \left[K \left[\frac{\partial}{\partial S} \left(\frac{\partial U_n}{\partial S} + KU_t \right) \right] + K^2 + \left(P + \frac{1}{\bar{I}} \right) \left(\frac{\partial U_t}{\partial S} - KU_n \right) + P - FDK + F \cos \theta_0 \right] \delta U_t \right\}_{S=0} \\ & + \left\{ \left[-\frac{\partial}{\partial S} \left(\frac{\partial U_n}{\partial S} + KU_t \right) - K + FD \right] \delta \left[\frac{\partial U_n}{\partial S} \right] \right\}_{S=1} \\ & + \left\{ \left[\frac{\partial}{\partial S} \left[\frac{\partial}{\partial S} \left(\frac{\partial U_n}{\partial S} + KU_t \right) + K \right] - P \left(\frac{\partial U_n}{\partial S} + KU_t \right) \right] \delta U_n \right\}_{S=1} \\ & + \left\{ \left[-K \left[\frac{\partial}{\partial S} \left(\frac{\partial U_n}{\partial S} + KU_t \right) \right] - K^2 - \left(P + \frac{1}{\bar{I}} \right) \left(\frac{\partial U_t}{\partial S} - KU_n \right) + P + FDK \right] \delta U_t \right\}_{S=1} = 0 \end{aligned} \quad (19)$$

2.2.2 Linearized Dynamic Model of the Support Structure

The static equilibrium configuration of the elastica arch depends on the values of f and d , or alternatively, on the non-dimensional variables F and D . For a tension-aligned structure, F and D are design variables; the value of F depends on the tension desired in the hinged panel array, and the value of D depends on the stiffness of the slender rod (elastica arch) and the difference in lengths of the hinged panel array and the slender rod. Assuming that the values of F and D are provided, static equilibrium configuration and pre-stress distribution can be obtained by substituting $U_t = U_n = 0$ in Eqs.(16) and (17) and solving for $K(S)$, $P(S)$, and θ_0 . A closed-form solution to this nonlinear static problem involves elliptic integrals of the first kind and can be found in [23].

Then Raleigh-Ritz method [27] was used to obtain the linearized dynamic model of the elastica arch about its static equilibrium configuration. To write the differential equations, one can substitute the equilibrium values of $P = P(S)$ and $K = K(S)$ into Eqs.(12) and (13), which yields the non-dimensional linear vibration equations

$$-\frac{\partial^3}{\partial S^3} \left(\frac{\partial U_n}{\partial S} + KU_t \right) + \frac{\partial}{\partial S} \left[P \left(\frac{\partial U_n}{\partial S} + KU_t \right) \right] + K \left(P + \frac{1}{I} \right) \left(\frac{\partial U_t}{\partial S} - KU_n \right) = \frac{\partial^2 U_n}{\partial T^2} \quad (20)$$

$$K \left[\frac{\partial^2}{\partial S^2} \left(\frac{\partial U_n}{\partial S} + KU_t \right) \right] + \frac{\partial}{\partial S} \left[\left(P + \frac{1}{I} \right) \left(\frac{\partial U_t}{\partial S} - KU_n \right) \right] - KP \left(\frac{\partial U_n}{\partial S} + KU_t \right) = \frac{\partial^2 U_t}{\partial T^2} \quad (21)$$

To solve Eqs.(20) and (21), one needs to go back to the energy form. Substituting the equilibrium values of $P = P(S)$ and $K = K(S)$ into the non-dimensional version of Eqs.(12) and (13), and then substituting the results in the non-dimensional form of the kinetic and strain energies in Eqs.(10) and (11), neglecting terms that have degree three and higher of variables U_n and U_t and their spatial derivatives, yield the following expressions for the non-dimensional kinetic and strain energies

$$\begin{aligned} \bar{\Pi}_V = \frac{1}{2} \int_0^1 & \left\{ \overbrace{K^2 + P^2 I}^{\text{terms 1 and 2}} + \overbrace{2K \frac{\partial}{\partial S} \left(\frac{\partial U_n}{\partial S} + KU_t \right) + 2P \left(\frac{\partial U_t}{\partial S} - KU_n \right)}^{\text{terms 3 and 4}} \right. \\ & \left. + \left[\frac{\partial}{\partial S} \left(\frac{\partial U_n}{\partial S} + KU_t \right) \right]^2 + \left(P + \frac{1}{I} \right) \left(\frac{\partial U_t}{\partial S} - KU_n \right)^2 + P \left(\frac{\partial U_n}{\partial S} + KU_t \right)^2 \right\} dS \quad (22) \end{aligned}$$

$$\bar{\Pi}_T = \frac{1}{2} \int_0^1 \left\{ \left(\frac{\partial^2 U_n}{\partial T^2} \right)^2 + \left(\frac{\partial^2 U_t}{\partial T^2} \right)^2 \right\} dS \quad (23)$$

Note that $\bar{\Pi}_V$ and $\bar{\Pi}_T$ are related to Π_V and Π_T , respectively, by the relations

$$\bar{\Pi}_V = \frac{L}{EI} \Pi_V, \quad \bar{\Pi}_T = \frac{L}{EI} \Pi_T$$

In Eq.(22), terms 1 and 2 of the integrand are functions of S alone, and not a function of time.

The same is true for terms 3 and 4 since a variation of the integral of these terms can be shown to be zero. The first four terms of Eq.(22) therefore result in constant strain energy, which does not contribute to the vibration of the system.

Assuming U_n and U_t to be of the form

$$U_n(S, T) = V_n(S) e^{i\omega T}, \quad U_t(S, T) = V_t(S) e^{i\omega T} \quad (24)$$

where $V_n(S)$ and $V_t(S)$ are the mode shapes, the mode shapes are discretized as follows:

$$V_n(S) = \sum_i W_{n,i}(S) Y_i = W_n(S) \cdot Y \quad (25)$$

$$V_t(S) = \sum_i W_{t,i}(S) Z_i = W_t(S) \cdot Z \quad (26)$$

where $W_n(S)$ and $W_t(S)$ are vectors of known shape functions. They are constructed using piece-wise polynomials (cubic and linear, respectively), standard in finite element discretizations, with discontinuities at nodes. Y and Z are vectors of nodal degrees of freedom (see Eq.(??) below) associated with V_n and V_t . Substituting Eqs.(24), (25) and (26) into Eqs.(22) and (23), one can rewrite the non-dimensional kinetic and strain energies as follows:

$$\bar{\Pi}_V = \frac{e^{i2\omega T}}{2} [Y^T \quad Z^T] \mathbb{K}_A \begin{bmatrix} Y \\ Z \end{bmatrix} + Const \quad (27)$$

$$\bar{\Pi}_T = \frac{e^{i2\omega T}}{2} (-\omega^2) [Y^T \quad Z^T] \mathbb{M}_A \begin{bmatrix} Y \\ Z \end{bmatrix} \quad (28)$$

where

$$Const = \frac{1}{2} \int_0^1 \left\{ K^2 + P^2 \bar{I} + 2K \frac{\partial}{\partial S} \left(\frac{\partial U_n}{\partial S} + K U_t \right) + 2P \left(\frac{\partial U_t}{\partial S} - K U_n \right) \right\} dS \quad (29)$$

is the constant strain energy associated with the static equilibrium configuration, discussed before. Using this form the mass and stiffness matrices \mathbb{M}_A and \mathbb{K}_A of the elastica arch (support structure) were assembled.

2.2.3 Hinged Panel Array

The array of hinged panels is shown in Fig.5. It was modelled using a standard finite element method. Two-dimensional two-node frame elements were employed with three degrees of freedom at each node: two translational and one rotational degrees of freedom. A geometric stiffness matrix was added to the standard frame stiffness matrix to model the effect of tension f . A hinge between two panels is treated as a node in the finite element model. The left and right elements of the hinge node have independent rotations but have common translations. The mass and stiffness matrices are assembled as \mathbb{M}_P and \mathbb{K}_P .

The the hinged panel array is then assembled with the elastica arch by connecting their ends together using pin joints. In the modelling, that is to assemble \mathbb{M}_A with \mathbb{M}_P and assemble \mathbb{K}_A with



Figure 5: The array of hinged panels

\mathbb{K}_P . After assembly, the end nodes of the two substructures share translations in the plane but maintain independent rotational degrees of freedom.

2.2.4 Methods of Stiffness Variation

Stiffness variation described by Eq.(2) was realized in the assembled tension-aligned structure by two methods. These two methods are depicted in Fig.6 and are described below:

- (A) The rotations of two adjacent panels at their common hinge, θ_P^k and θ_P^{k+1} , are connected by a rotational spring of time-varying stiffness.
- (B) Node i on the elastica arch and node j on the panel array are connected by a translational spring of time-varying stiffness.

Method (A) can be implemented by placing an electromagnetic brake at the hinge of the adjacent panels. Turning on the brake prevents relative rotation between the adjacent panels and is equivalent to constraining the degrees of freedom θ_P^k and θ_P^{k+1} by a rotational spring of very high stiffness. Turning off the brake releases the degrees of freedom and is equivalent to setting the spring stiffness to zero. Method (B) can be implemented by connecting and disconnecting an elastic bar between a point on the arch and a point on the panel. These two points were chosen to coincide with nodes of the finite element model for the purpose of simulation.

The stiffness of the tension-aligned structure can be varied using multiple springs of the type described in method (A) and/or method (B). Since each of these springs can be in one of two states, the tension-aligned structure have multiple stiffness states. In the next section, where simulation results are presented, the stiffness of the structure was switched cyclically between the lowest stiffness state and the highest stiffness state via intermediate stiffness states. The lowest and highest stiffness states are defined as the states with the lowest and the highest fundamental frequency.

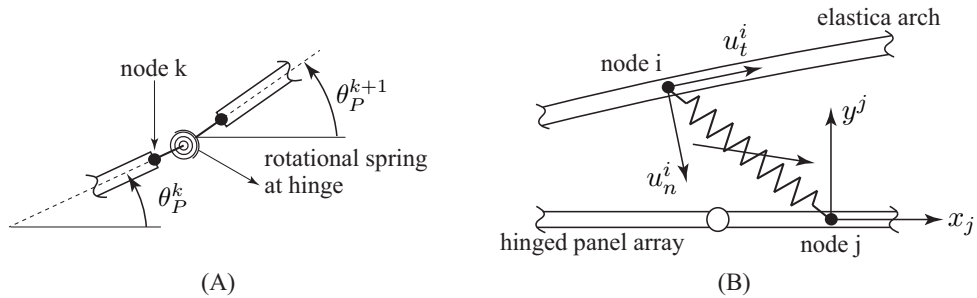


Figure 6: Stiffness variation in the tension-aligned structure is realized using two methods: (A) and (B); these are described in section 3.4.

Table 1: Properties of Simulated Tension-Aligned Structure

Material	Aluminum
Young's modulus E	69×10^9 Pa
Density $\bar{\rho}$	2700 kg/m^3
Damping ratio ζ	0.001
Panel number	8
Panel length L_p	1.000 m
Panel area $b \times h$	$0.500 \text{ m} \times 0.015 \text{ m}$
Radius of support rod r	0.040 m
Length of support rod L	8.000 m approx.
Eccentricity of connection d	0.008 m
Tension f	1000 N

2.2.5 Numerical Simulation

The material and geometric properties of the tension-aligned structure are provided in Table 1. The structure is made of aluminum and the damping ratio of all modes is assumed to be $\zeta = 0.001$. The panel array is comprised of eight panels of dimensions $L_p \times b \times h$; these dimensions are shown in Fig.7. Each panel is modelled using 10 beam elements. The support structure (elastica arch) is initially a straight rod of radius 0.04 m and length ≈ 8.00 m. It is modelled using 80 elements. The eccentricity of the load applied to the support structure is 0.008 m. The tension in the hinged panel array was assumed to be 1000 N. This is less than 5% of the buckling load of the straight rod with free-free boundary conditions. In the following of this subsection, the behavior of the structure without control, and with control using two different methods of stiffness variation was simulated.

With an initial condition where the second joint of the hinged panel array (see Fig.7) was displaced vertically by 0.01 m (1% of the length of the panel array) and released, the first 25 modes of the structure were simulated; these do not include the rigid-body modes. The energy of the tension-aligned structure is shown in Fig.8 for three different cases, as described below:

1. Unconstrained structure (no control) undergoing free vibration,

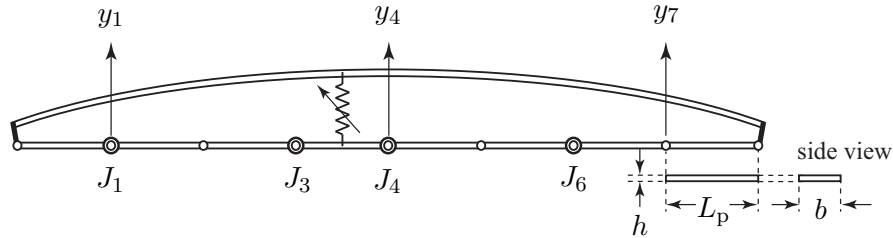


Figure 7: The eight-panel tension-aligned structure used in simulations.

2. Constrained structure (no control) with high-stiffness rotational spring in joints J_1 , J_3 , J_4 and J_6 - see Fig.7. Using method (A) of stiffness variation, the stiffness of the rotational springs was activated when the adjacent panels were aligned. The rotational springs were activated at the earliest possible opportunity in a sequential manner and were kept in their high stiffness state.
3. Controlled structure with switched stiffness using method (A). The high-stiffness rotational springs in joints J_1 , J_3 , J_4 and J_6 were activated sequentially when their adjacent panels were aligned and their stiffness were then set to zero simultaneously. The process was repeated 92 times in the simulation period of 180 sec.

It is clear from Fig.8 that the energies of the unconstrained structure and the constrained structure decayed slowly compared to the structure with switched stiffness. After 180 sec, the unconstrained structure and the constrained structure had $\approx 22.5\%$ of their initial energy left; in contrast, the structure with switched stiffness had $\approx 0.4\%$ of its initial energy left. Although vibration energy was dissipated through internal damping in all three cases, the structure with switched stiffness has higher rate of energy dissipation since it effectively funnels energy from the low-frequency modes to the high-frequency modes.

For the structure with switched stiffness, the joints were released simultaneously, not sequentially, to reduce the time required for each cycle of constraint application and removal. In simulations, where high-stiffness springs were used to constrain the joints, simultaneous release of the joints caused residual energy stored in the springs to vanish. This discontinuous change in the energy, was however not the main mechanism of energy dissipation. A bookkeeping of this energy over all cycles indicates that it did not exceed 0.1% of the total energy at its initial level. This means the bulk of the energy was dissipated due to energy transfer from low-frequency modes to high-frequency modes. In practical implementation [22], where electromagnetic brakes may be used to constrain the joints, release of the brakes will not result in direct loss of energy (since brakes do not store energy) but facilitate energy transfer to the high-frequency modes where they will be dissipated quickly.

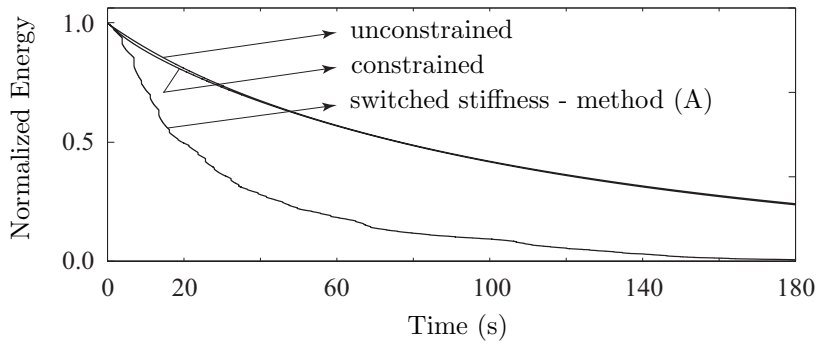


Figure 8: Plot of energy for the three cases discussed in section 4.2.

The rates of energy decay of the unconstrained structure and the constrained structure were almost identical. Since the structure has many degrees-of-freedom and activating the springs in four joints only makes it marginally stiffer than the unconstrained structure. This can be verified

from Table 2 which shows the first six natural frequencies of the unconstrained and constrained structures.

Table 2: First six natural frequencies of the unconstrained and the constrained tension-aligned structure in rad/s.

Unconstrained	ω_1	ω_2	ω_3	ω_4	ω_5	ω_6
	3.820	6.999	9.129	13.144	15.859	20.213
Constrained	$\bar{\omega}_1$	$\bar{\omega}_2$	$\bar{\omega}_3$	$\bar{\omega}_4$	$\bar{\omega}_5$	$\bar{\omega}_6$
	3.996	7.502	11.096	28.042	37.875	71.666

The structure with switched stiffness, where stiffness was varied using method (A), had a faster rate of energy decay than the uncontrolled (unconstrained and constrained) structures.

In order to further improve the efficiency of the control using switched stiffness, different methods of stiffness variation need to be investigated. Applying methods (A) and (B), again using 25 modes, the behavior of the structure was simulated for the same initial condition that was used in the previous case. The energy of the tension-aligned structure is shown in Fig.9 for the following three cases:

1. Unconstrained structure undergoing free vibration,
2. Structure with switched stiffness using method (A). The high-stiffness rotational springs in joints J_1 , J_3 , J_4 and J_6 were activated sequentially when their adjacent panels were aligned and their stiffness were then set to zero simultaneously. The process was repeated 92 times within the simulation period of 180 sec.
3. Structure with switched stiffness using methods (A) and (B). The high-stiffness rotational springs in joints J_1 , J_3 , and J_4 were activated sequentially when their adjacent panels were aligned. This was followed by connecting an elastic bar (high-stiffness translational spring) between a point on the elastica arch and a point on the panel array (see Fig.7) in a manner such that no energy was added to the structure. The stiffness of all four springs were then set to zero simultaneously. The process was repeated 105 times within the simulation period of 180 sec.

It is clear from Fig.9 that the energy of the uncontrolled structure decayed slowly compared to the structure with switched stiffness. After 180 sec, the uncontrolled structure had $\approx 22.5\%$ of its initial energy left; in contrast, the structure with switched stiffness using method (A) had $\approx 0.4\%$ of its initial energy left. For vibration suppression to $\approx 0.4\%$ energy level, methods (A) and (B) combined requires 76 sec as compared to 180 sec required by method (A). Accordingly, for the case of methods (A) and (B) combined, the transverse displacements of three points on the hinged panel array Fig.10, which clearly shows the suppression of vibration.

The efficiency of vibration suppression using stiffness variation can be much improved by combining methods (A) and (B). This improvement in effectiveness can be understood by examining the modal disparity matrices for the two cases and comparing their modal disparity indices. The

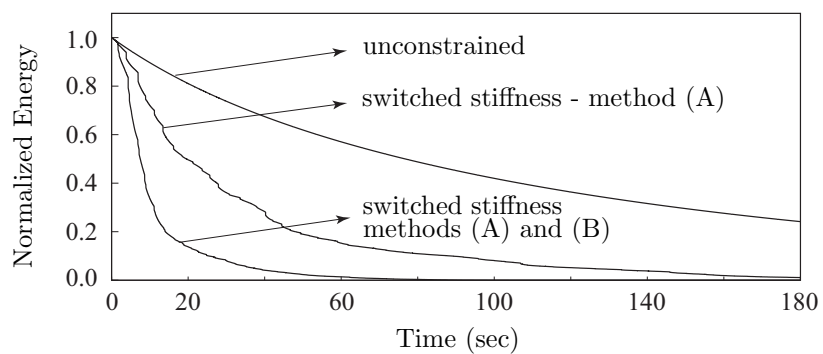


Figure 9: Plot of energy for the three cases discussed in section 4.3.

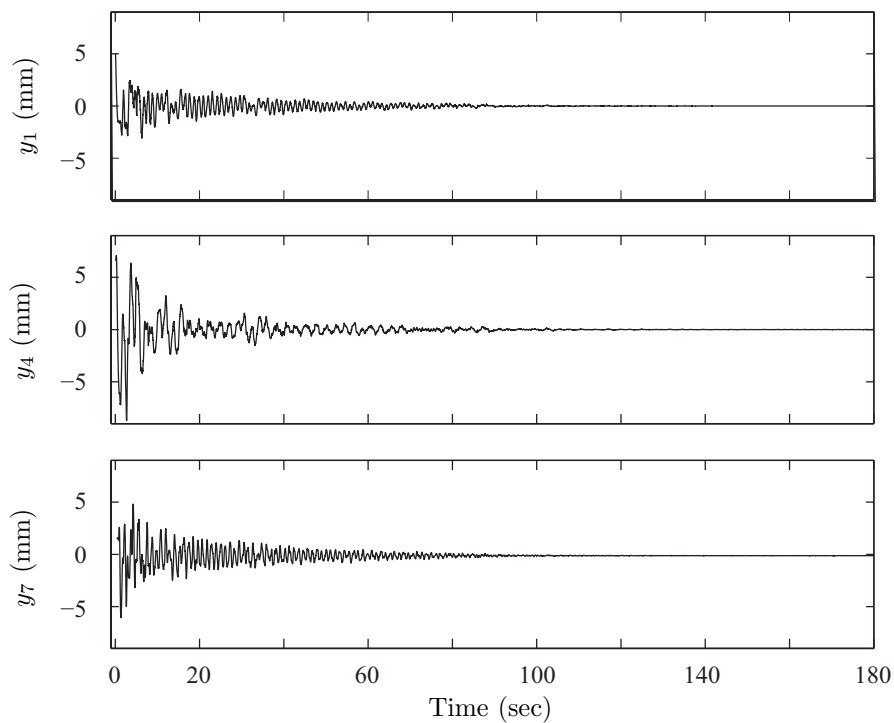


Figure 10: Plots of y_1 , y_4 and y_7 (see Fig.7) - the transverse displacements of three points on the hinged panel array.

modal disparity indices for these two cases were computed as

$$\lambda_A = 22.15, \quad \lambda_{AB} = 40.48 \quad (30)$$

Since λ_{AB} is greater than λ_A , stiffness variation combining methods (A) and (B) is more effective than method (A) in transferring energy from the low-frequency modes to the high-frequency modes. Modal disparity proves to be a effective measure to evaluate the magnitude of stiffness variation for the purpose of vibration suppression.

2.3 Model of a Three-Dimensional Simple Tension-Aligned Structure

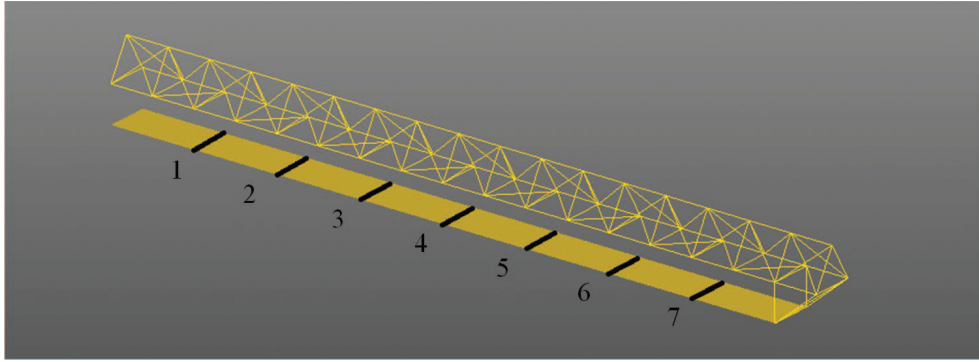


Figure 11: Overview of the tension-aligned three-dimensional structure. 8 panels are connected using 7 hinges and supported by a truss structure.

A three-dimensional model was built to verify the effectiveness of the stiffness variation method in a more realistic structure. This model takes the design data of the truss structure from the ISAT project and was set all material to be aluminum. 17 truss cells were built. Each cell has the dimension of 0.5 m and the truss structure has the total length of 8.5 m. The truss functions as a support structure and provides tension for the hinged panel array where the antenna is mounted. There are 8 panels hinged to form an array and each panel has the dimension of 1.00 m \times 0.50 m \times 0.01 m. The overview of structure is shown in Fig.11. The combined structure is clamped at one end and free at another. The tension level was set to be 200 N. Geometry of the structure is depicted in Fig.12.

The finite element package **ANSYS** was used for the finite element modelling. The truss structure was modelled using link element that has two nodes and three degrees of freedom at each node. The plates were modelled using shell element that has four nodes and six degrees of freedom at each node. In total the DOF number is 648 and 25 modes were used in the dynamic simulation.

Only method (A) was used in this model for the application of stiffness variation. The control logic was similar with the two-dimensional model. Results of vibration suppression are very consistent, as shown in Fig.13. When four hinges were used, the energy plot resembles the results of the two-dimensional model. As the number of controlled hinges increases, vibration suppression gets more efficient. This is because the magnitude of the modal disparity increases as the number of controlled hinges increases.

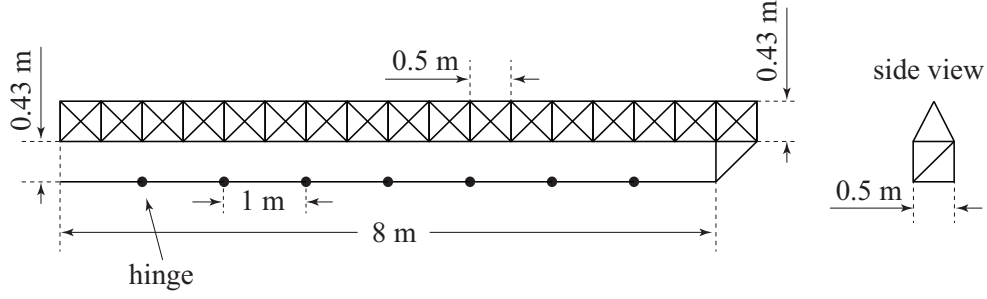


Figure 12: Geometry of the three-dimensional structure.

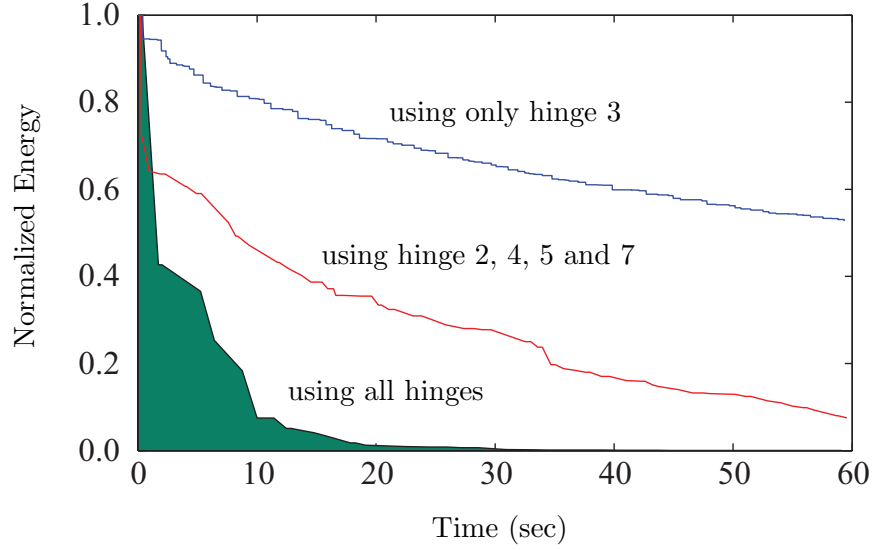


Figure 13: Plots of energy for cases of controlling different number of joints.

3 Vibration Suppression Through Sliding Mechanism

In this section we discuss the second control strategy for vibration suppression. This strategy is different from the first control strategy in that the location of the constraint does not change discretely from one point in the structure to another but moves continuously. The strategy is verified in simulations using a moving slider than constrains the transverse displacement of the antenna, modeled as a nonlinear beam, relative to the support structure, which is assumed to be rigid.

3.1 Equations of Motion for a Nonlinear Beam with a Fixed Slider

Similar to Sec. 2.2.1, the planar vibration model of the nonlinear beam was derived following the work by Perkins [23] on the elastica arch. Consider a slender beam shown in Fig.14, held in equilibrium under horizontal end load f , where f can be either tensile or compressive (less than the buckling load). The beam is initially straight and measured to have length L under f . Both

ends of the beam are subsequently pinned to the ground; this creates pre-stress in the beam. A frictionless slider is assumed to constrain the motion of the beam; its location is fixed in space that initially coincides with the midpoint of the beam. The slider restricts the position of the material point on the beam in contact with it, but does not restrict the slope of the beam. Since the slider is fixed and does not move with the beam, material can flow through it. A point Q on the beam instantaneously in contact with the constraint can be described using material coordinate $s = s_q$, where s is measured in the initial equilibrium configuration using Lagrangian description (material coordinate). Due to a disturbance, a point on the beam has displacement of $\vec{u}(s, t)$, where t denotes time. $\vec{u}(s, t)$ can be decomposed into tangential component $\vec{u}_t(s, t)$ which is always horizontal and normal component $\vec{u}_n(s, t)$ which is always vertical. Note that two sets of coordinates are used here, namely, the material coordinate system s and the X - Y frame.

The sliding constraints can be described as

$$C_1 = u_n(s = s_q, t) = 0 \quad (31)$$

$$C_2 = u_t(s = s_q, t) + s_q(t) - L/2 = 0 \quad (32)$$

where Eq.(31) states that any material point in contact with the constraint should never have vertical motion. Equation (32) states that the material point Q in contact with the slider is initially measured as s_q in the initial equilibrium configuration, and that point Q has a horizontal displacement of u_t in order to meet the constraint imposed by the slider.

Using Kirchhoff's assumptions for beam deformation [24], with the consideration that the beam remains straight in its equilibrium configuration, the nonlinear axial strain can be written as [26]

$$e = -f/EA + \frac{\partial u_t}{\partial s} + \frac{1}{2} \left[\left(\frac{\partial u_t}{\partial s} \right)^2 + \left(\frac{\partial u_n}{\partial s} \right)^2 \right] \quad (33)$$

The curvature k can be expressed as [25]

$$k = \frac{\partial^2 u_n}{\partial s^2} \quad (34)$$

where A , E , and I denote the cross-sectional area, Young's modulus, and area moment of inertia

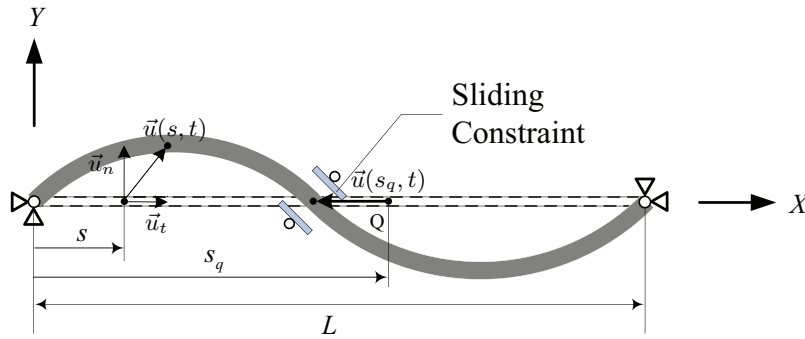


Figure 14: A pinned-pinned beam with a sliding constraint.

of the beam, respectively. The virtual work done by internal elastic forces due to any virtual deformation can be written as

$$\int_{\Omega} \sigma \delta[\varepsilon] d\Omega = \int_0^L EAe\delta[e] ds + \int_0^L EI k \delta[k] ds \quad (35)$$

where σ and ε represent general stress and strain, respectively. Ω is the domain of interest which include all material points on the beam.

Using the principle of virtual displacement and D'Alembert's principle, together with Lagrange multipliers yield the dynamics of the beam in the following form

$$\int_{\Omega} \sigma \delta[\varepsilon] + (-\mathbf{P} + \rho \ddot{\mathbf{u}}) \cdot \delta[\mathbf{u}] d\Omega = \delta[\lambda \cdot \mathbf{C}] \quad (36)$$

where vector \mathbf{P} is the external force, \mathbf{u} is the displacement field, $(\dot{})$ is the derivative with respect to T , λ is a vector of Lagrange multipliers, and \mathbf{C} is the vector of constraint expressions. The term on the right hand side of Eq.(36) can be expanded as

$$\lambda \cdot \mathbf{C} = \lambda_1 C_1 + \lambda_2 C_2 \quad (37)$$

where the expressions for C_1 and C_2 are given in Eqs.(31) and (32). Since Lagrange multipliers have the physical interpretations of constraint forces, λ_1 and λ_2 represent the constraint forces in vertical and horizontal directions, respectively.

Equation (36) states that the beam is in dynamic equilibrium if the external virtual work done by the applied forces equal the internal virtual work done by the forces for any virtual deformation which satisfies the kinematic boundary conditions. Here, the internal virtual work is extended with an inertial term using D'Alembert's principle, and kinematic boundary conditions for constraints are included by application of Lagrange multipliers.

In the problem of interest, \mathbf{P} is only used in setting up the static problem to create the initial condition. As far as the dynamic problem is in concern, one can simply set external forces to be zero. Namely $\mathbf{P} = 0$.

Substituting Eqs.(33) and (34) into Eq.(35), then substituting the resulting equation together with Eqs.(31), (32), (37), and $\mathbf{P} = 0$ into Eq.(36), and using the following non-dimensional quantities

$$\begin{aligned} S &\triangleq \frac{s}{L}, & S_Q &\triangleq \frac{s_q}{L}, & U_t &\triangleq \frac{u_t}{L}, & U_n &\triangleq \frac{u_n}{L}, & K &\triangleq kL \\ F &\triangleq \frac{fL^2}{EI}, & \bar{I} &\triangleq \frac{I}{AL^2}, & T &\triangleq \frac{t}{(\rho L^4/EI)^{1/2}}, & \Lambda &\triangleq \frac{\lambda L^2}{EI} \end{aligned} \quad (38)$$

gives the energy form of the equations of motion

$$\begin{aligned}
& \int_0^1 \ddot{U}_n \delta[U_n] dS + \int_0^1 \ddot{U}_t \delta[U_t] dS + \int_0^1 \frac{\partial^2 U_n}{\partial S^2} \delta \left[\frac{\partial^2 U_n}{\partial S^2} \right] dS \\
& + \int_0^1 \left(-F + \frac{1}{\bar{I}} \frac{\partial U_t}{\partial S} + \frac{1}{2\bar{I}} \left(\frac{\partial U_t}{\partial S} \right)^2 + \frac{1}{2\bar{I}} \left(\frac{\partial U_n}{\partial S} \right)^2 \right) \frac{\partial U_n}{\partial S} \delta \left[\frac{\partial U_n}{\partial S} \right] dS \\
& + \int_0^1 \left(-F + \frac{1}{\bar{I}} \frac{\partial U_t}{\partial S} + \frac{1}{2\bar{I}} \left(\frac{\partial U_t}{\partial S} \right)^2 + \frac{1}{2\bar{I}} \left(\frac{\partial U_n}{\partial S} \right)^2 \right) \left(1 + \frac{\partial U_t}{\partial S} \right) \delta \left[\frac{\partial U_t}{\partial S} \right] dS \quad (39) \\
& = \left\{ \Lambda_1 \frac{\partial U_n(S=S_Q)}{\partial S} + \Lambda_2 \left(\frac{\partial U_t(S=S_Q)}{\partial S} + 1 \right) \right\} \delta[S_Q] \\
& + U_n(S=S_Q) \delta[\Lambda_1] + \{U_t(S=S_Q) + S_Q - 1/2\} \delta[\Lambda_2] \\
& + \Lambda_1 \delta[U_n(S=S_Q)] + \Lambda_2 \delta[U_t(S=S_Q)]
\end{aligned}$$

Integrating Eq.(39) by parts and collecting like terms of independent variations yield the differential form of equations of motion and boundary conditions. The PDE's are written as the following: from collecting terms involving $\delta[U_n]$

$$\begin{aligned}
& -\frac{\partial^4 U_n}{\partial S^4} - F \frac{\partial^2 U_n}{\partial S^2} + \frac{3}{2\bar{I}} \left(\frac{\partial U_n}{\partial S} \right)^2 \frac{\partial^2 U_n}{\partial S^2} + \frac{1}{2\bar{I}} \frac{\partial^2 U_n}{\partial S^2} \left(\frac{\partial U_t}{\partial S} \right)^2 + \frac{1}{\bar{I}} \frac{\partial U_n}{\partial S} \frac{\partial U_t}{\partial S} \frac{\partial^2 U_t}{\partial S^2} \\
& + \frac{1}{\bar{I}} \frac{\partial^2 U_n}{\partial S^2} \frac{\partial U_t}{\partial S} + \frac{1}{\bar{I}} \frac{\partial U_n}{\partial S} \frac{\partial^2 U_t}{\partial S^2} + \Lambda_1 \mathcal{D}(S_Q - S) = \frac{\partial^2 U_n}{\partial T^2} \quad (40)
\end{aligned}$$

from collecting terms involving $\delta[U_t]$

$$\begin{aligned}
& \left(-F + \frac{1}{\bar{I}} \right) \frac{\partial^2 U_t}{\partial S^2} + \frac{3}{2\bar{I}} \left(\frac{\partial U_t}{\partial S} \right)^2 \frac{\partial^2 U_t}{\partial S^2} + \frac{1}{\bar{I}} \frac{\partial U_n}{\partial S} \frac{\partial U_t}{\partial S} \frac{\partial^2 U_n}{\partial S^2} + \frac{1}{2\bar{I}} \left(\frac{\partial U_n}{\partial S} \right)^2 \frac{\partial^2 U_t}{\partial S^2} \\
& + \frac{3}{\bar{I}} \frac{\partial U_t}{\partial S} \frac{\partial^2 U_t}{\partial S^2} + \frac{1}{\bar{I}} \frac{\partial U_n}{\partial S} \frac{\partial^2 U_n}{\partial S^2} + \Lambda_2 \mathcal{D}(S_Q - S) = \frac{\partial^2 U_t}{\partial T^2} \quad (41)
\end{aligned}$$

from collecting terms involving $\delta[S_Q]$

$$\Lambda_1 \frac{\partial U_n(S=S_Q, T)}{\partial S} + \Lambda_2 \frac{\partial U_t(S=S_Q, T)}{\partial S} + \Lambda_2 = 0 \quad (42)$$

together with the recovered constraint equations in non-dimensional form

$$U_n(S=S_Q, T) = 0 \quad (43)$$

$$U_t(S=S_Q, T) + S_Q - 1/2 = 0 \quad (44)$$

where in Eqs.(40) and (41) $\mathcal{D}(S_Q - S)$ is the Dirac delta function.

Eqs.(40) - (44) are a full set of equations of motion describing the dynamics of a nonlinear beam with a fixed slider, where no energy is dissipated. If damping is added to the system, Eq.(36) needs

to be rewritten to include the viscous damping terms, such as

$$\int_{\Omega} \sigma \delta[\varepsilon] + \eta \dot{\sigma} \delta[\varepsilon] + (-\mathbf{P} + \rho \ddot{\mathbf{u}}) \cdot \delta[\mathbf{u}] d\Omega = \delta[\lambda \cdot \mathbf{C}] \quad (45)$$

where the added term $\eta \dot{\sigma} \delta[\varepsilon]$ expresses that the internal damping forces contribute to the virtual work due to any virtual deformation of the structure. It also states that the damping force is proportional to the damping coefficient η and the strain rate $\dot{\sigma}$.

Starting from Eq.(45), and repeating the process of nondimensionalization and variation process described above, one can get another set of equations of motion with damping presented.

3.2 Variable-Length Finite Element Method

The finite element model of the system was established in the framework of the Arbitrary Lagrange-Euler (ALE), following the work of [19]. To discretize Eq.(39) using finite element method that takes into account the sliding nature of the constraint, a sliding node was chosen to put on the beam in the same position coinciding with the constraint, which does not move in space when the constraint is fixed. Therefore, this special node is described using Eulerian description. As for other nodes, where the Lagrangian description is used, nodes are attached to certain material points chosen at the beginning, and material coordinates of those nodes will remain the same as time progresses [32].

Because of the existence of the special sliding node, two neighboring elements that share this node become variable-length elements, while other elements are still regular. It is necessary to derive expressions of velocity and acceleration of any material point in a variable-length element, which compared to regular elements, are more complicated.

Consider a standard 2-node, 6-dof frame element described by material coordinates of the two nodes (S_1^e, S_2^e) and 6 nodal displacements $(U_{n1}^e, U_{n1}^{'e}, U_{t1}^e, U_{n2}^e, U_{n2}^{'e}, U_{t2}^e)$, where the superscript e indicates element-wise or local numbering is used. In the framework of ALE description, both (S_1^e, S_2^e) and $(U_{n1}^e, U_{n1}^{'e}, U_{t1}^e, U_{n2}^e, U_{n2}^{'e}, U_{t2}^e)$ can vary with time. Using Hermite polynomials for shape functions of displacement in the normal direction $U_n^e(S, T)$, one obtains

$$U_n^e(S, T) = \mathbf{N}_e^T(S, S_1^e(T), S_2^e(T)) \mathbf{q}_n^e(T) \quad (46)$$

where

$$\mathbf{N}_e = \begin{pmatrix} 2\xi^3 - 3\xi^2 + 1 \\ \xi^3 - 2\xi^2 + \xi \\ -2\xi^3 + \xi^2 \\ \xi^3 - \xi^2 \end{pmatrix}, \quad \mathbf{q}_n^e = \begin{pmatrix} U_{n1}^e \\ U_{n1}^{'e} \\ U_{n2}^e \\ U_{n2}^{'e} \end{pmatrix} \triangleq \begin{pmatrix} a_1^e \\ b_1^e \\ a_2^e \\ b_2^e \end{pmatrix} \quad (47)$$

and $\xi = (S - S_1^e)/(S_2^e - S_1^e)$. The shape functions \mathbf{N}_e are functions of both material coordinate S and node locations (S_1^e, S_2^e) , which means \mathbf{N}_e are functions of S and T . The nodal displacements \mathbf{q}_n^e are functions of time T .

Similarly, with the help of Lagrange polynomials, the tangential displacement $U_t^e(S, T)$ can be written as

$$U_t^e(S, T) = \mathbf{R}_e^T(S, S_1^e(T), S_2^e(T)) \mathbf{q}_t^e(T) \quad (48)$$

where

$$\mathbf{R}_e = \begin{pmatrix} (S_2^e - S)/(S_2^e - S_1^e) \\ (S - S_1^e)/(S_2^e - S_1^e) \end{pmatrix}, \quad \mathbf{q}_t^e = \begin{pmatrix} U_{t1}^e \\ U_{t2}^e \end{pmatrix} \triangleq \begin{pmatrix} c_1^e \\ c_2^e \end{pmatrix} \quad (49)$$

The shape functions \mathbf{R}_e^T are functions of S and T . The nodal displacements \mathbf{q}_t^e are functions of time T .

Differentiating Eqs.(46) and (48) twice with respect to time, the accelerations can be derived as

$$\begin{aligned} \ddot{U}_n^e = & \mathbf{N}_e^T \ddot{\mathbf{q}}_n^e + \frac{\partial \mathbf{N}_e^T}{\partial S_1^e} \mathbf{q}_n^e \ddot{S}_1^e + \frac{\partial \mathbf{N}_e^T}{\partial S_2^e} \mathbf{q}_n^e \ddot{S}_2^e + 2 \frac{\partial \mathbf{N}_e^T}{\partial S_1^e} \dot{\mathbf{q}}_n^e \dot{S}_1^e + 2 \frac{\partial \mathbf{N}_e^T}{\partial S_2^e} \dot{\mathbf{q}}_n^e \dot{S}_2^e \\ & + \frac{\partial^2 \mathbf{N}_e^T}{\partial S_1^{e2}} \mathbf{q}_n^e \dot{S}_1^{e2} + 2 \frac{\partial^2 \mathbf{N}_e^T}{\partial S_1^e \partial S_2^e} \mathbf{q}_n^e \dot{S}_1^e \dot{S}_2^e + \frac{\partial^2 \mathbf{N}_e^T}{\partial S_2^{e2}} \mathbf{q}_n^e \dot{S}_2^{e2} \end{aligned} \quad (50)$$

$$\begin{aligned} \ddot{U}_t^e = & \mathbf{R}_e^T \ddot{\mathbf{q}}_t^e + \frac{\partial \mathbf{R}_e^T}{\partial S_1^e} \mathbf{q}_t^e \ddot{S}_1^e + \frac{\partial \mathbf{R}_e^T}{\partial S_2^e} \mathbf{q}_t^e \ddot{S}_2^e + 2 \frac{\partial \mathbf{R}_e^T}{\partial S_1^e} \dot{\mathbf{q}}_t^e \dot{S}_1^e + 2 \frac{\partial \mathbf{R}_e^T}{\partial S_2^e} \dot{\mathbf{q}}_t^e \dot{S}_2^e \\ & + \frac{\partial^2 \mathbf{R}_e^T}{\partial S_1^{e2}} \mathbf{q}_t^e \dot{S}_1^{e2} + 2 \frac{\partial^2 \mathbf{R}_e^T}{\partial S_1^e \partial S_2^e} \mathbf{q}_t^e \dot{S}_1^e \dot{S}_2^e + \frac{\partial^2 \mathbf{R}_e^T}{\partial S_2^{e2}} \mathbf{q}_t^e \dot{S}_2^{e2} \end{aligned} \quad (51)$$

Substituting Eqs.(46)-(51) into Eq.(39) gives the finite element version of the dynamic system. The beam is meshed with $2m$ number of elements, and there are m elements to the left and m elements to the right of the constraint. Thus node $m + 1$ is the sliding node on the beam and is fixed in space. This special node has the material coordinate S_Q that varies with time, while other nodes have fixed material coordinates. Now one can use generalized coordinates \mathbf{q} , a vector with $6m + 4$ entries written as

$$\mathbf{q} = (a_1, a_2, \dots, a_{2m+1}, b_1, b_2, \dots, b_{2m+1}, c_1, c_2, \dots, c_{2m+1}, S_Q)^T \quad (52)$$

$$\begin{aligned} & \int_0^1 \ddot{U}_n \frac{U_n}{\mathbf{q}} \delta[\mathbf{q}] dS + \int_0^1 \ddot{U}_t \frac{U_t}{\mathbf{q}} \delta[\mathbf{q}] dS + \int_0^1 \frac{\partial^2 U_n}{\partial S^2} \frac{\partial \left(\frac{\partial^2 U_n}{\partial S^2} \right)}{\partial \mathbf{q}} \delta[\mathbf{q}] dS \\ & + \int_0^1 \left(-F + \frac{1}{I} \frac{\partial U_t}{\partial S} + \frac{1}{2I} \left(\frac{\partial U_t}{\partial S} \right)^2 + \frac{1}{2I} \left(\frac{\partial U_n}{\partial S} \right)^2 \right) \frac{\partial U_n}{\partial S} \frac{\partial \left(\frac{\partial U_n}{\partial S} \right)}{\partial \mathbf{q}} \delta[\mathbf{q}] dS \\ & + \int_0^1 \left(-F + \frac{1}{I} \frac{\partial U_t}{\partial S} + \frac{1}{2I} \left(\frac{\partial U_t}{\partial S} \right)^2 + \frac{1}{2I} \left(\frac{\partial U_n}{\partial S} \right)^2 \right) \left(1 + \frac{\partial U_t}{\partial S} \right) \frac{\partial \left(\frac{\partial U_t}{\partial S} \right)}{\partial \mathbf{q}} \delta[\mathbf{q}] dS \\ & = \left\{ \Lambda_1 \frac{\partial U_n(S = S_Q)}{\partial S} + \Lambda_2 \left(\frac{\partial U_t(S = S_Q)}{\partial S} + 1 \right) \right\} \delta[S_Q] \\ & + U_n(S = S_Q) \delta[\Lambda_1] + \{ U_t(S = S_Q) + S_Q - 1/2 \} \delta[\Lambda_2] \\ & + \Lambda_1 \delta[U_n(S = S_Q)] + \Lambda_2 \delta[U_t(S = S_Q)] \end{aligned} \quad (53)$$

Variation of the terms in Eq.(39) is carried out by taking derivatives with respect to \mathbf{q} . Now the finite element version of the dynamic system is given as Eq.(53).

With the help of Lagrange multipliers, one can treat all variables in \mathbf{q} independent with each other, then by collecting coefficients of arbitrary $\delta[\mathbf{q}]$, Eq.(53) gives rise to $(6m + 4)$ nonlinear equations.

Geometric boundary conditions given by pinned-pinned

$$\begin{aligned} U_n(S = 0) = U_t(S = 0) = U_n(S = 1) = U_t(S = 1) = 0 \\ \text{or } a_1 = c_1 = a_{2m+1} = c_{2m+1} = 0 \end{aligned} \quad (54)$$

cancel 4 equations out of $(6m + 4)$. In total, $(6m)$ equations are obtained regarding $\ddot{\mathbf{q}}$. They can be written as

$$\mathbf{M}(\mathbf{q}, T)_{(6m \times 6m)} \ddot{\mathbf{q}}_{(6m)} = \mathbf{F}(\mathbf{q}, \dot{\mathbf{q}}, T)_{(6m \times 6m)} \quad (55)$$

where \mathbf{M} is the generalized mass matrix and \mathbf{F} is the generalized force vector.

Furthermore, by collecting coefficients of $\delta[\Lambda_1]$ and $\delta[\Lambda_2]$, two constraint equations can be recovered as

$$\begin{aligned} C_1 = a_{m+1} &= 0 \\ C_2 = c_{m+1} + S_{m+1} - 1/2 &= 0 \end{aligned} \quad (56)$$

These form a set of differential algebraic equations which describe the motion of the beam. If damping is presented, one can follow the whole process starting from Eq.(45), then obtain a discretized dynamic system with the form very similar to Eq.(55). The process is lengthy and not repeated here. Together with 2 constraint equations expressed in Eqs.(56), it is shown that the system has been successfully discretized using variable-length finite elements.

Table 3: Properties and geometry of the simulated beam with a sliding constraint.

Material	Aluminum
Young's modulus E	69×10^9 Pa
Density $\bar{\rho}$	2700 kg/m ³
Damping coefficient η	10^{-5} sec
Beam length L	3.66 m
Beam cross section area	38.1 mm \times 1.57 mm
Pre-load f	0 N

A numeric simulation of free vibration was given to demonstrate the effectiveness of the mathematical model. Geometry and material properties used in the simulation are listed in Table 3. In the numeric model, the beam was meshed using 20 frame elements. A sliding joint, node No. 11 was placed on the beam at the same position where the constraint was located, with the unknown material coordinate S_Q . There were 10 elements to the left and 10 elements to the right of the sliding node. Elements No. 10 and 11 were variable-length elements while other elements were regular which had nodes with fixed coordinates allocated at the beginning. Initial conditions were

created by applying a 5 N positive vertical force on the beam at $S = 0.75$ or $s = 2.743$ m. Eqs.(56) and (55) were formulated and numerically integrated by time to solve for $\mathbf{q}(T)$, $\dot{\mathbf{q}}(T)$, $\Lambda_1(T)$ and $\Lambda_2(T)$ as time progresses. This process was done using MATLAB solver `ode15s`. The results are shown in Fig.15.

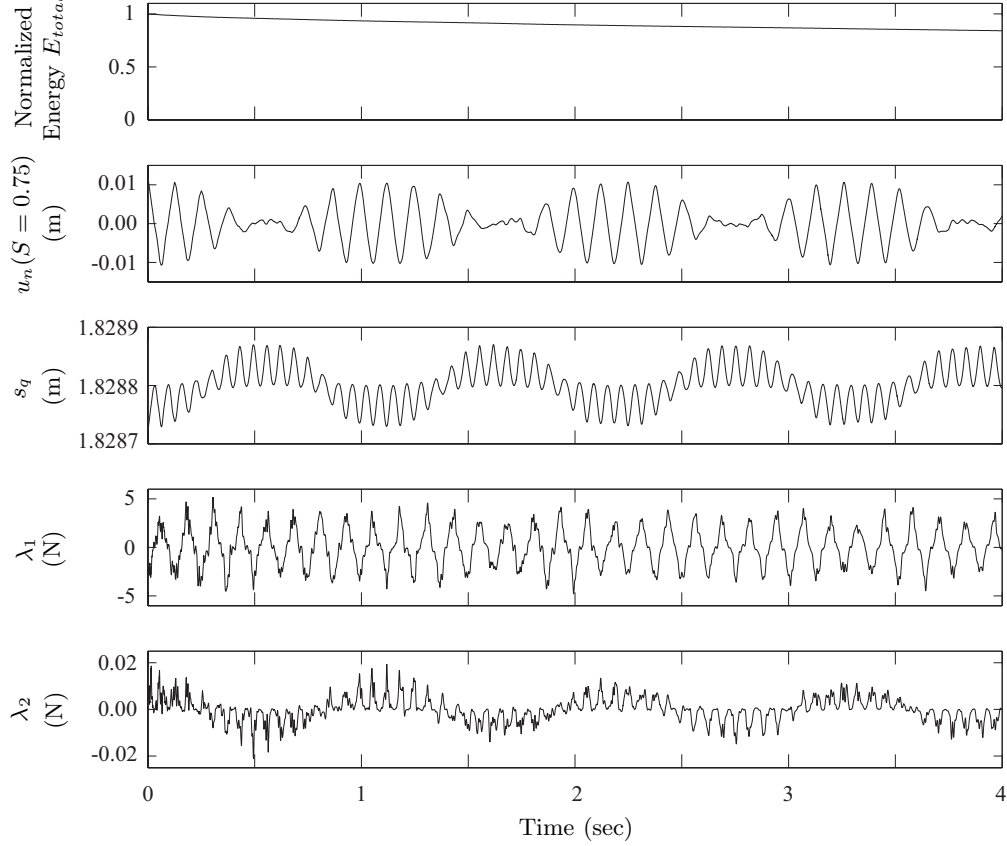


Figure 15: Plots of the system in free vibration: normalized energy; transverse displacement u_n sampled at $S = 0.75$ or $s = 2.743$ m; material coordinate s_q of the point Q in contact with the slider; constraint force λ_1 in vertical direction; constraint force λ_2 in horizontal direction.

The oscillatory behavior of the nonlinear beam can be clearly observed from Fig.15. Frequency of the transverse displacement u_n sampled at $S = 0.75$ is approximately twice the frequency of material coordinate s_q corresponding to the point Q in contact with the slider. Frequency of the constraint force λ_1 in vertical direction is strongly associated with the transverse vibration $u_n(S = 0.75)$, while frequency of the constraint force λ_2 in horizontal direction is strongly associated with s_q . Constraint forces also carries high frequency components. This is due to the fact that constraint force is related to higher degrees of derivatives of u_n and u_t with respect to s . Total energy of the system was obtained by combining kinetic and strain energies and then normalized by the initial level. Energy decayed slowly due to the presence of light viscous damping with the damping coefficient being $\eta = 1 \times 10^{-5}$ sec.

3.3 Feedback Control Design

3.3.1 Preliminary Design of Slider Motion Control

The control strategy is based on the idea of negative work. This idea simply states that energy loss of the beam can be caused by negative work done by the constraint force from the slider. When the slider is fixed in space, no actual work is done by the constraint force and the total energy of the system is only dissipated through material damping, as shown in simulation results in the free vibration case. Since one can measure (in practice) or compute (in simulation) the horizontal constraint force Λ_2 , it can be used as feedback in the control scheme. Instead of using a fixed constraint, one can prescribe the slider's horizontal motion X_C to be opposite to the direction of Λ_2 such that it does negative work. This strategy was realized by putting a new constraint to replace the one in Eq.(32).

$$V_C = \dot{X}_C = \frac{\partial (U_t(S = S_Q, T) + S_Q(T))}{\partial T} \quad (57)$$

The constraint in Eq.(31) remains the same.

This control scheme is shown in Fig.16. Based on previous work done by Nudehi, et al. [33] and Issa, et al. [34], the Lyapunov candidate is chosen as

$$V_1 = E_{total}(\mathbf{q}, \dot{\mathbf{q}}, T) \quad (58)$$

The origin of V_1 corresponds to the static equilibrium state of the beam. It is obvious that when the beam is staying in static equilibrium, i.e., $\mathbf{q} = \dot{\mathbf{q}} = 0$, there is $V_1 = 0$. The change of total energy can only be caused by damping and the work done by the horizontal constraint force Λ_2 if one prescribes the horizontal position X_C of the slider while keeping its vertical position always 0, namely

$$\dot{E}_{total} = \dot{E}_{damping} + \dot{X}_C \Lambda_2 \quad (59)$$

where $\dot{E}_{damping} \leq 0$. To implement this control scheme, material boundary was set since in practice the slider can only operate within a certain range of the beam. In order to realize $S_{lower} \leq S_Q \leq S_{upper}$, there is

$$-\dot{X}_C = u = \begin{cases} h(y_1 = \Lambda_2) & \text{if } S_{lower} < y_2 < S_{upper} \\ 0 & \text{otherwise} \end{cases} \quad (60)$$

Substituting Eqs.(59) and (60) into Eq.(58) yields

$$\dot{V}_1 = \begin{cases} \dot{E}_{damping} - uy_1 = \dot{E}_{damping} - y_1 h(y_1) \leq 0 & \text{if } S_{lower} < y_2 < S_{upper} \\ \dot{E}_{damping} \leq 0 & \text{otherwise} \end{cases} \quad (61)$$

For the choice of control input in Eq.(60), it has been shown in Eq.(61) that it leads to $\dot{V}_1 \leq 0$. Using LaSalle's Theorem [35], one can claim that the origin is asymptotically stable.

Efficacy of the control design in Eq.(60) was investigated by simulation. The beam was meshed using 20 elements, with the same properties and geometry shown in Table 3. $s_{lower} = 1.33$ m and

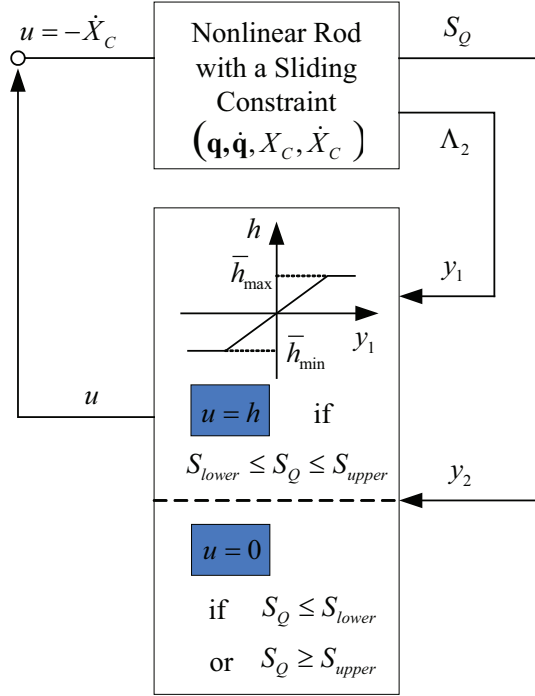


Figure 16: Preliminary feedback control design.

$s_{upper} = 2.33$ m were set for the simulation. In implementation, the material range $[s_{lower}, s_{upper}]$ for control was determined by the stroke length of the sliding device. The speed limit of the slider was set to be 1 m/sec. With the same initial conditions applied as in the previous subsection, results are shown in Fig.17.

As shown in Fig.17, at the end of 12 sec, the total energy of the system was effectively dissipated to 1.0% of its starting level, while the transverse displacement at $S = 0.75$ was reduced to 17%. Most high frequency vibration has been suppressed, as the history of $u_n(S = 0.75)$ shows, leaving the beam with slowly-varying transverse oscillations that should be fairly easy to cope with in application. The range of motion for the slider stayed within 0.2 m, which suggests that a relatively small travel distance suffices for the purpose of vibration suppression in this design. As the vibration energy was dissipated and the displacement of the beam was reduced, constraint force λ_2 in horizontal direction decreased fast. This is due to that the geometric nonlinearity which gives rise to λ_2 becomes less significant as the reduced amplitude of u_n decouples the interaction between u_n and u_t in the axial strain. One potential problem of the preliminary control design is that because of the high frequency components in λ_2 , the position of the slider oscillates too fast in order to follow the change of λ_2 , as one can see from the plot of \dot{x}_c . This may exceed the bandwidth of the actuator. The potential issue in implementation led to the modified feedback control design.

3.3.2 Modified Control Design

As stated in last subsection, when the slider is trying to follow the change of Λ_2 , it may oscillates too fast that the hardware requirement exceeds the bandwidth of the actuator. To attack this problem,

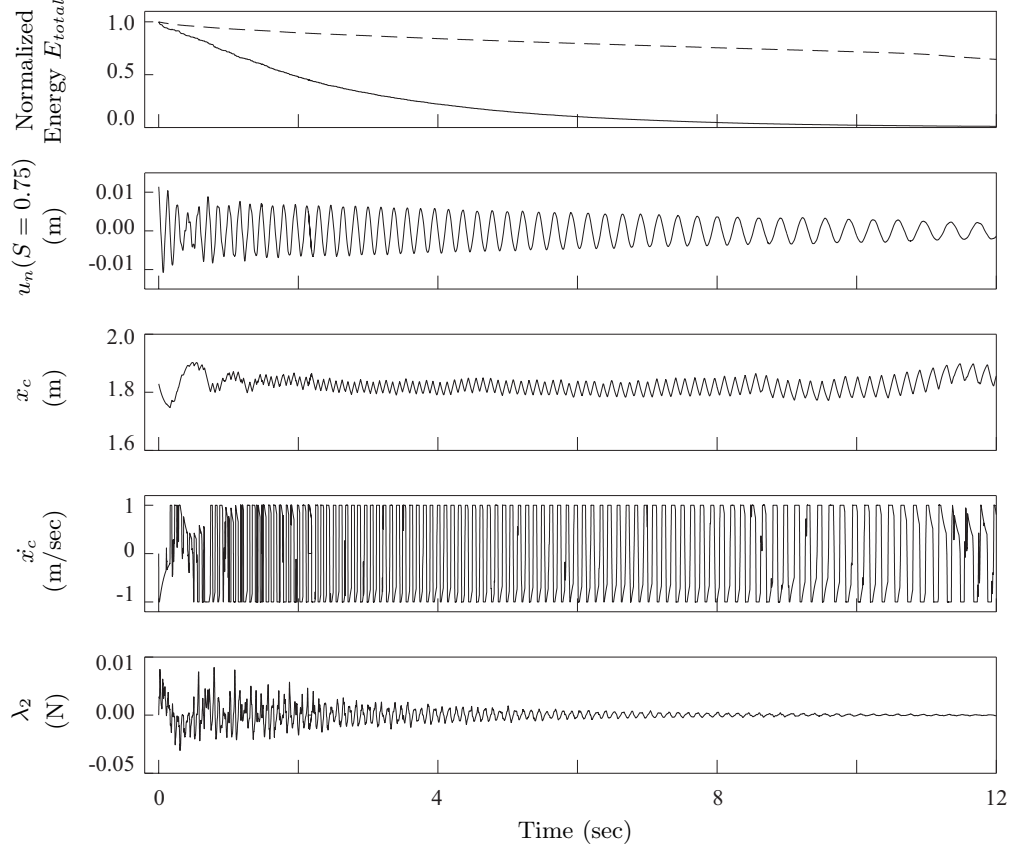


Figure 17: Plots of the system applied with direct control: normalized energy of the direct control results in solid line, normalized energy of free vibration in dashed line as reference; transverse displacement u_n sampled at $S = 0.75$ or $s = 2.743$ m; slider position x_c ; slider velocity \dot{x}_c ; constraint force λ_2 in horizontal direction.

introduce a Low-Pass Filter (LPF) was introduced into the feedback loop, which measures Λ_2 as its input and gives a signal z as the output. This LPF is chosen to be first-order with the time constant τ . Instead of using Λ_2 directly in the control law, the filtered signal z was used in the modified feedback control design. Choosing a new Lyapunov candidate, one can prove that the stability of the modified system can be retained.

The modified control scheme is shown in Fig. 18. A new Lyapunov candidate was chosen as

$$V_2 = E_{total} + \tau \int_0^z h(\xi) d\xi \quad (62)$$

The origin of V_2 corresponds to the static equilibrium state of the beam when $\mathbf{q} = \dot{\mathbf{q}} = \Lambda_2 = 0$. Use Eq.(59) one can obtain that when $S_{lower} < y_2 < S_{upper}$, the following holds

$$\begin{aligned} \dot{V}_2 &= \dot{E}_{total} + \tau h(z) \dot{z} \\ &= \dot{E}_{damping} - y_1 u + h(y_1 - z) \\ &= \dot{E}_{damping} - z h \leq 0 \end{aligned} \quad (63)$$

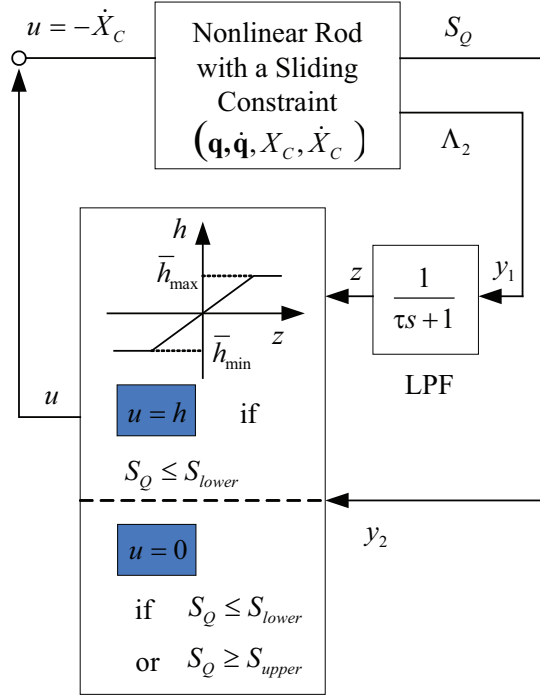


Figure 18: Modified control design with filter.

And when $y_2 \leq S_{lower}$ or $y_2 \geq S_{upper}$, there is $\dot{V}_2 = \dot{E}_{damping} \leq 0$. Therefore using LaSalle's Theorem, again one can claim that the origin is asymptotically stable for the modified control system.

The efficacy of the modified control design was investigated by simulation. Meshing, material properties, geometric and control parameters, plus initial conditions were chosen to be the same as in the preliminary control design. For the first-order low-pass filter, time constant τ was simulated as 40 ms. Results of simulation are shown in Fig.19.

Adding the low-pass filter is a trade-off between control efficiency and actuator bandwidth. As shown in Fig.19, the slider velocity \dot{x}_c driven by the actuator, switched less frequently compared with the preliminary design results, especially at the early stage (before 2 sec). This eases the requirement for the actuator bandwidth. The cost for this is that the vibration suppression process becomes less efficient. At the end of 12 sec, the total energy of the system had 9.7% remained. To achieve the same level of 1.0% suppression as in the control without filter, the modified design obviously requires longer time of the slider application.

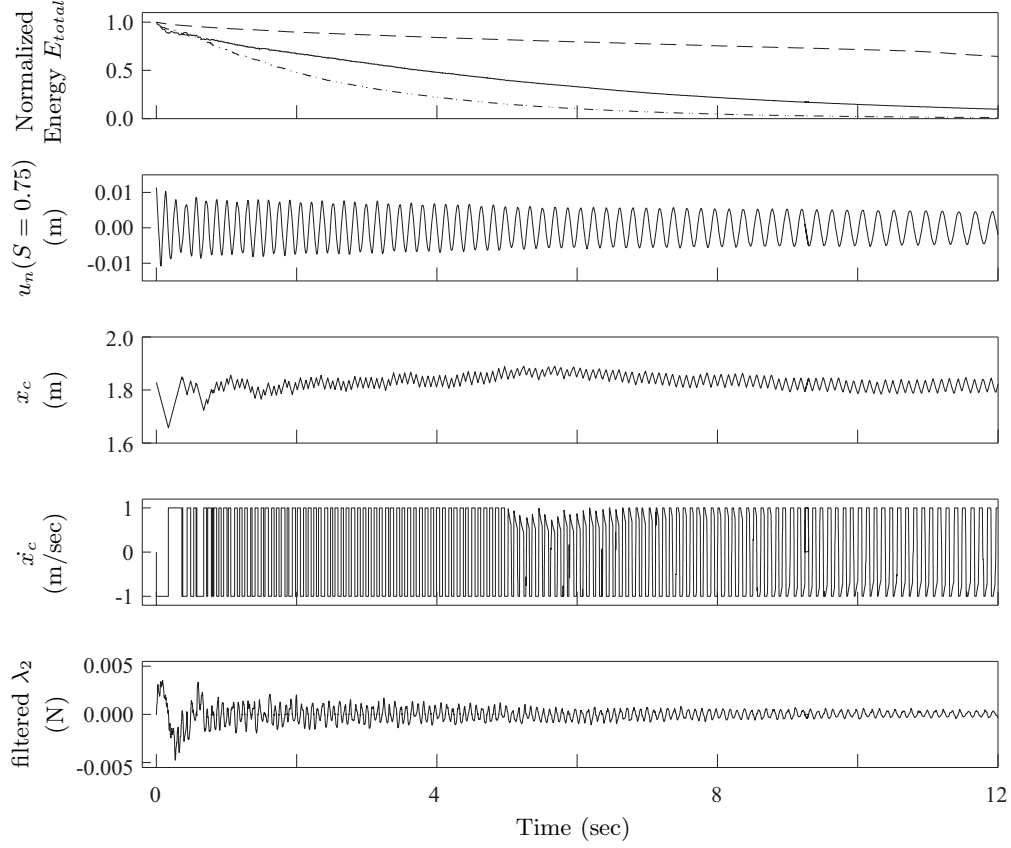


Figure 19: Plots of the system applied with direct control: normalized energy of the modified control results in solid line, normalized energy of free vibration in dashed line as reference, normalized energy of the direct control results in dotted-solid line as reference; transverse displacement u_n sampled at $S = 0.75$ or $s = 2.743$ m; slider position x_c ; slider velocity \dot{x}_c ; constraint force λ_2 in horizontal direction after the low-pass filter.

4 Vibration Suppression Through Boundary Tension Variation

In this section we present the third control strategy for vibration suppression. The antenna is modeled as a thin plate and it is connected to the support structure via distributed tensile forces along its boundary.

4.1 Dynamics of a Rectangular Plate Subject to Tension

Consider a rectangular Kirchhoff-Love plate with the dimension of $a \times b$. The equation of the transverse vibration subject to in-plane stress is given as [27]:

$$D \left[\frac{\partial^4 w}{\partial x^4} + 2 \frac{\partial^4 w}{\partial x^2 \partial y^2} + \frac{\partial^4 w}{\partial y^4} \right] + \bar{\rho} h \frac{\partial^2 w}{\partial t^2} = f + N_x \frac{\partial^2 w}{\partial x^2} + N_y \frac{\partial^2 w}{\partial y^2} + 2N_{xy} \frac{\partial^2 w}{\partial x \partial y} \quad (64)$$

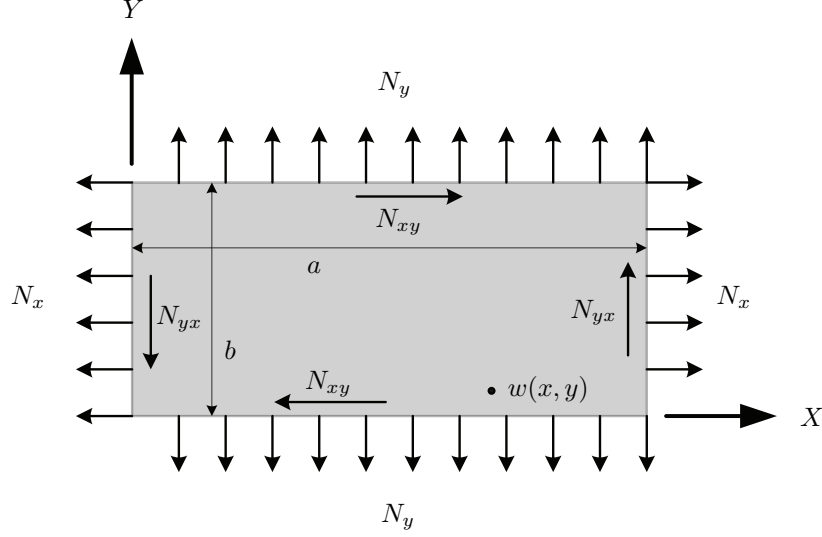


Figure 20: Plate subject to tension

where the rigidity is defined as

$$D \triangleq \frac{Eh^3}{12(1-\nu^2)} \quad (65)$$

and $w = w(x, y, t)$ denotes the transverse displacement of a material point (x, y) at time t ; f denotes the transverse load; $\bar{\rho}$ and h are the material density and plate thickness, respectively; N_x , N_y and N_{xy} are normal and shear in-plane stress, as shown in Fig.20.

Kinetic and strain energies of the plate can be written as

$$T \triangleq \frac{1}{2} \int \int \bar{\rho} h \dot{w}^2 \, dx dy \quad (66)$$

$$U \triangleq \frac{1}{2} \int \int [D \{ (\frac{\partial^2 w}{\partial x^2} + \frac{\partial^2 w}{\partial y^2})^2 + 2(1-\nu) \left[(\frac{\partial^2 w}{\partial x \partial y})^2 - \frac{\partial^2 w}{\partial x^2} \frac{\partial^2 w}{\partial y^2} \right] \} + N_x (\frac{\partial^2 w}{\partial x^2})^2 + N_y (\frac{\partial^2 w}{\partial y^2})^2 + 2N_{xy} \frac{\partial w}{\partial x} \frac{\partial w}{\partial y}] \, dx dy \quad (67)$$

Assume w to be the form of

$$w(x, y, t) = W(x, y) e^{i\omega t} \quad (68)$$

where $W(x, y)$ is the mode shape. The modes shape is discretized as follows

$$W(x, y) = \sum_{k=1}^N c_k \phi_k(x, y) \quad (69)$$

where c_k is the generalized coordinates and ϕ_k are a series of basis functions. If the finite element analysis is used, ϕ_k are piece-wise polynomials known as shape functions. Here Rayleigh-Ritz method was employed and ϕ_k can be as simple as a series of sine functions for the simply supported

boundary condition.

Writing the maximum kinetic and strain energies as:

$$T_{max} = \frac{\omega^2}{2} X_p^T M_p X_p \quad (70)$$

$$U_{max} = \frac{1}{2} X_p^T K_p X_p \quad (71)$$

gives the generalized coordinates as

$$X_p = [c_1, c_2 \dots, c_N]^T \quad (72)$$

and the mass and stiffness matrices are assembled as

$$M_p(i, j) \triangleq \bar{\rho} h \int \int \phi_i \phi_j dx dy \quad (73)$$

$$K_p(i, j) \triangleq \int \int \left\{ D \left[\frac{\partial^2 \phi_i}{\partial x^2} \frac{\partial^2 \phi_j}{\partial x^2} + \frac{\partial^2 \phi_i}{\partial y^2} \frac{\partial^2 \phi_j}{\partial y^2} + \nu \frac{\partial^2 \phi_i}{\partial x^2} \frac{\partial^2 \phi_j}{\partial y^2} + \nu \frac{\partial^2 \phi_i}{\partial y^2} \frac{\partial^2 \phi_j}{\partial x^2} + 2(1 - \nu) \frac{\partial^2 \phi_i}{\partial x \partial y} \frac{\partial^2 \phi_j}{\partial x \partial y} \right] \right. \\ \left. + \underbrace{N_x \frac{\partial \phi_i}{\partial x} \frac{\partial \phi_j}{\partial x} + N_y \frac{\partial \phi_i}{\partial y} \frac{\partial \phi_j}{\partial y} + N_{xy} \left(\frac{\partial \phi_i}{\partial x} \frac{\partial \phi_j}{\partial y} + \frac{\partial \phi_i}{\partial y} \frac{\partial \phi_j}{\partial x} \right)}_{\text{stress induced stiffness terms}} \right\} dx dy \quad (74)$$

and the stiffness matrix can be viewed as a combination of:

$$K_p = K_0 + \underbrace{N_x K_x + N_y K_y + N_{xy} K_{xy}}_{\text{stress induced stiffness terms}} \quad (75)$$

Set $N_{xy} = 0$ and only consider the normal in-plane stress cause by tension, the stiffness matrix becomes

$$K_p = K_0 + N_x K_x + N_y K_y \quad (76)$$

With damping presented, the distretized equations of motion of the plate can be written as

$$M_p \ddot{X}_p + D_p \dot{X}_p + K_0 X_p + N_x K_x X_p + N_y K_y X_p = 0 \quad (77)$$

where $D_p = \beta K_p$ is the damping matrix for structural damping with a positive coefficient β . M_p , K_0 , K_x , K_y and D_p are positive-definite symmetric matrices.

4.2 Feedback Control Design

4.2.1 Direct Active Control

The proposed control strategy is to vary the tension level $N_x(t)$ and $N_y(t)$ based on the states of the system X_p . The scheme is given as

$$N_x = \begin{cases} 0 & \text{if } \dot{X}_p^T K_x X_p < 0 \\ P_x & \text{if } \dot{X}_p^T K_x X_p \geq 0 \end{cases} \quad (78)$$

and

$$N_y = \begin{cases} 0 & \text{if } \dot{X}_p^T K_y X_p < 0 \\ P_y & \text{if } \dot{X}_p^T K_y X_p \geq 0 \end{cases} \quad (79)$$

where P_x and P_y take positive values since their directions are tensile. This scheme is illustrated with the help of Fig. 21

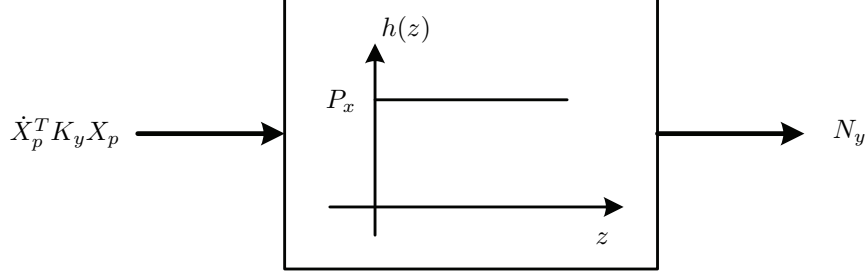


Figure 21: Diagram for the direct active control

Stability of this control scheme can be proven by choosing Lyapunov function candidate as

$$V_1 = \frac{1}{2} \dot{X}_p^T M_p \dot{X}_p + \frac{1}{2} X_p^T K_0 X_p \quad (80)$$

Then its time derivative is

$$\dot{V}_1 = -\dot{X}_p^T D_p \dot{X}_p - (\dot{X}_p^T K_x X_p) N_x - (\dot{X}_p^T K_y X_p) N_y \leq 0 \quad (81)$$

where the properties that D_p , K_x and K_y are positive-definite matrices are used. Using LaSalle's Theorem [35], one can claim that the origin is asymptotically stable.

Simulation was done to verify this control scheme. In the numerical simulation, a rectangular plate with the dimension $a \times b \times h$ being simply supported at four edges were considered. The basis functions in Eq.(69) were chosen to be

$$\phi(m, n) = \sin(mx\pi/a) \sin(ny\pi/b) \quad (82)$$

so that geometric boundary conditions were satisfied. Six terms of the basis functions were taken for the computation, they were arranged as: $\phi_1 = \phi(1, 1)$, $\phi_2 = \phi(2, 1)$, $\phi_3 = \phi(3, 1)$, $\phi_4 = \phi(1, 2)$, $\phi_5 = \phi(2, 2)$, $\phi_6 = \phi(3, 2)$. Initial condition was created by setting at $t = 0$

$$X_p = [1.00 \ 0.50 \ 0.25 \ 0.20 \ 0.02 \ 0.01]^T \times 10^{-2}$$

and $\dot{X}_p = 0$. This initial condition reasonably assigns more energy to lower frequency modes associated with ϕ_i terms that have small index i values. Other properties and parameters are shown in Table 4.

Table 4: Properties of Simulated Plate

Material	Aluminum
Young's modulus E	69×10^9 Pa
Density $\bar{\rho}$	2700 kg/m ³
Damping coefficient β	0.0002
Plate length a	5 m
Plate width b	2 m
Plate thickness h	0.001 m
Maximum Tension in x direction P_x	15 N/m
Maximum Tension in y direction P_y	6 N/m

Eq. (77) was rewritten in the first-order form and then integrated by time using MATLAB solver `ode15s` to implement the control scheme described in Eq. (78) and 79. Results are shown in Fig. 22.

Fig. 22 shows the efficacy of this active control design. In Fig. 22 (a), no control was applied and Lyapunov energy defined in Eq. (80) was dissipated only through internal material damping. At $t = 40$ s, there was 47% of the starting vibration energy remained in the plate. While as shown in Fig. 22 (b), remaining energy was negligible in the system and vibration was completely suppressed by this control strategy. Displacement plots sampled at one point on the plate are also shown in 22 (c) and (d). The comparison demonstrates the efficacy of the scheme.

This control scheme requires the tension varies based on the information of the system states, namely, generalized displacements and velocities obtained from an observer. This information is strongly associated with the modal amplitudes of the vibrating plate. Since there are high frequency components presented, it requires the tension switches directions fast enough to follow the change of system states. This may cause issues in physical implementation, given all hardware used to control the tension have limited bandwidth and speed. To address this issue, a modified control design was developed.

4.2.2 Modified Control Design

In order to maintain the control efficacy with limited bandwidth and speed of hardware, a Low-Pass Filter (LPF) was into the feedback loop of the control scheme, as shown in Fig. 23. This filter is first order with the time constant τ . It measures $\dot{X}_p^T K_x X$ and $\dot{X}_p^T K_y X$ as its inputs and gives a signal z as the output. There is also saturation considered in the model's transfer function. A parameter ϵ describes the linear response region and saturation region of the actuator.

One needs to guarantee the stability of this modified control design. Choosing the following Lyapunov candidate, one can prove that the stability of the modified system is retained:

$$V_2 = \frac{1}{2} \dot{X}_p^T M_p \dot{X}_p + \frac{1}{2} X_p^T K_0 X_p + \tau \int_0^z h(\sigma) d\sigma \quad (83)$$

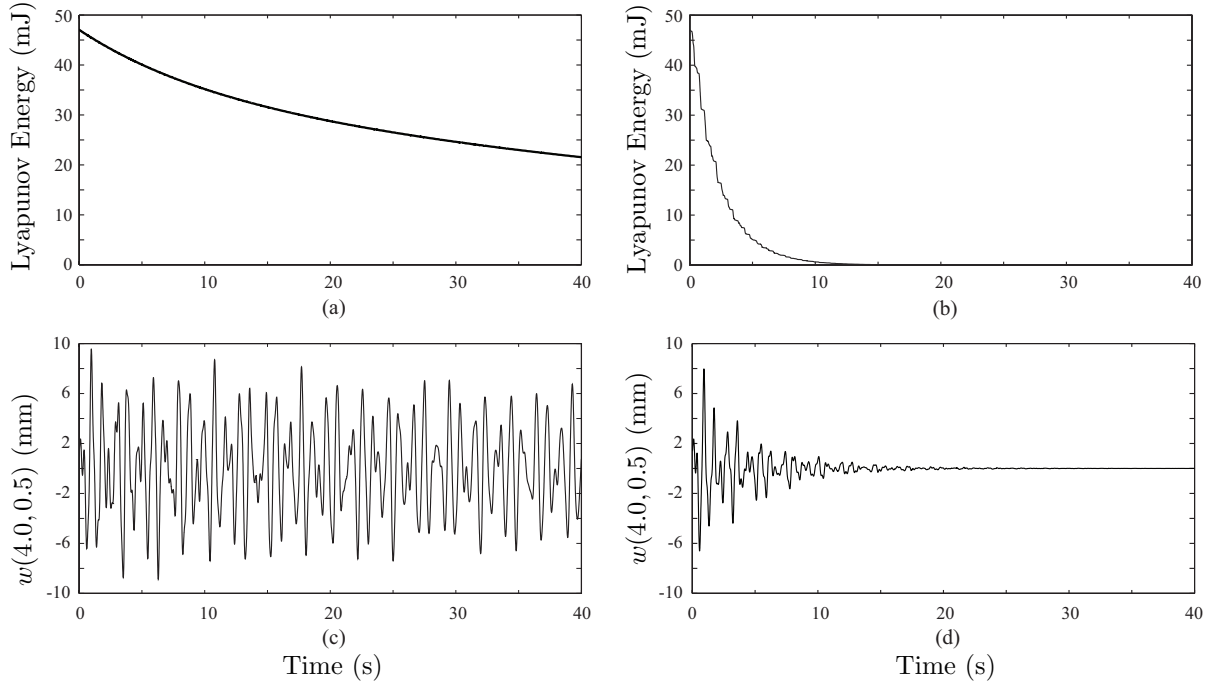


Figure 22: Simulation results of the direct active control design: (a)(b) Lyapunov energy of the uncontrolled and controlled systems; (c)(d) Transverse displacement of the uncontrolled and controlled systems, sampled at $(x = 4.0, y = 0.5)$

Time derivative of the Lyapunov function is

$$\dot{V}_2 = -\dot{X}_p^T D_p \dot{X}_p - (\dot{X}_p^T K_x X_p) N_x - (\dot{X}_p^T K_y X_p) N_y + \tau h(z) \dot{z} \quad (84)$$

$$= -\dot{X}_p^T D_p \dot{X}_p - (\dot{X}_p^T K_x X_p) N_x - (\dot{X}_p^T K_y X_p) N_y - z h \leq 0 \quad (85)$$

Using LaSalle's theorem, one can claim that this modified system is asymptotically stable.

Numerical verification was performed similarly as in the direct control design. Same basis functions constructed by sine series were employed. Properties and geometry are shown in Table 4. Time constant of the first-order filter was set to be $\tau = 0.2$ s and the saturation parameter $\epsilon = 0.3$. Same as in the direct control, boundaries are simply supported and initial condition was created

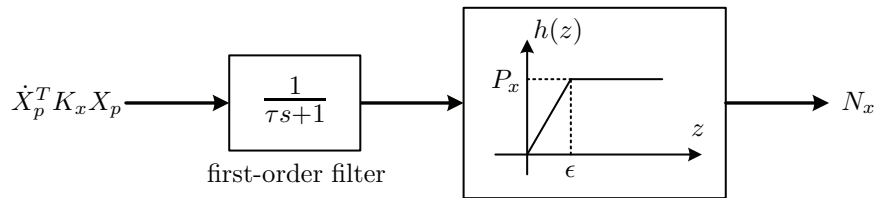


Figure 23: Diagram for the filtered control

by setting at $t = 0$

$$X_p = [1.00 \ 0.50 \ 0.25 \ 0.20 \ 0.02 \ 0.01]^T \times 10^{-2}$$

and $\dot{X}_p = 0$. Results are shown in Fig. 24.

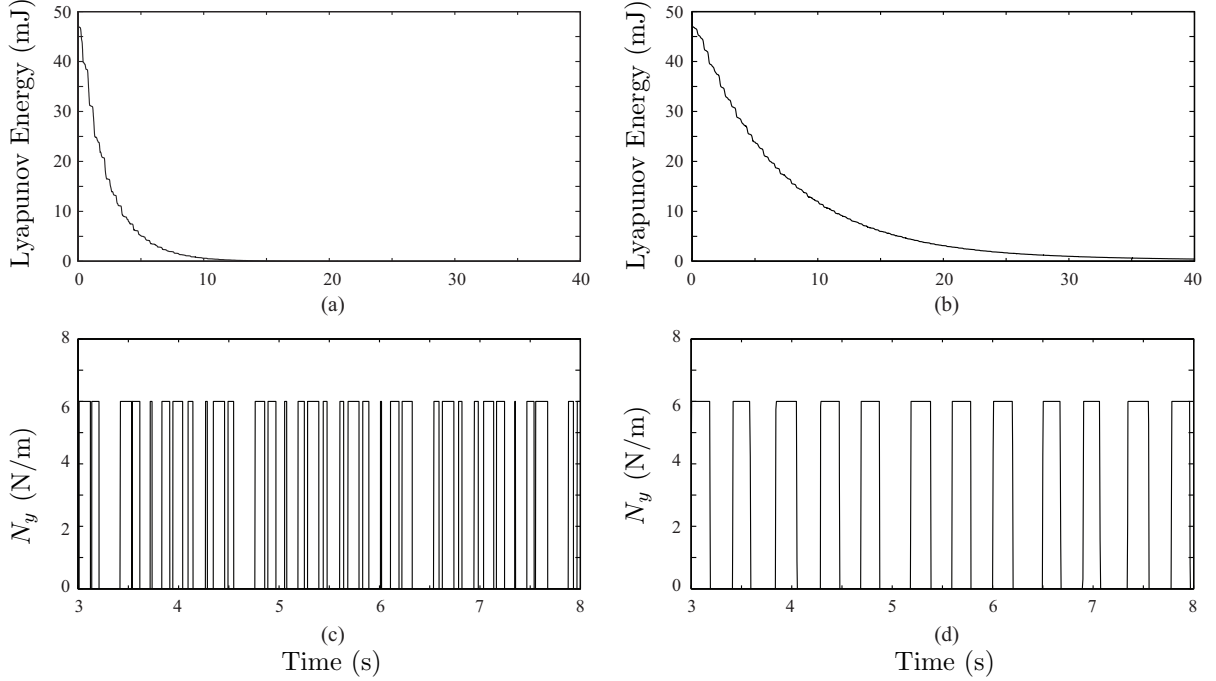


Figure 24: Comparison between the direct control and the filtered control results: (a)(b) Lyapunov energy of the direct and filtered controlled systems; (c)(d) y-direction tension level in the direct and filtered controlled systems

Fig. 24 provides the comparison between the direct control and the modified control with a filter. Fig. 24 (a) records the Lyapunov energy defined in Eq. (80) of the direct control system. The remaining level at $t = 40$, as discussed before, was negligible. Energy result of the modified system is shown in Fig. 22 (b). At $t = 40$ s, there was approximately 1% remained compared to the starting level. The control became less efficient with the filter added. This reveals the typical trade-off between the hardware cost and system performance. The high efficiency of the direct control comes with the cost of extremely high bandwidth and speed requirements of the hardware, in order to taken into account the high frequency modes of the plate and to follow them. Fig. 22 (c) and (d) compare part of the tension level history under two different control schemes. It clearly shows with the filter, actuator switches the direction of tension N_y much less frequently. Choosing $\tau = 0.2$ and $\epsilon = 0.3$ reasonably models the realistic speed of a control system. The balance was achieved with the modified design, considering the lower switching frequency but still satisfactory vibration suppression efficiency.

4.3 Boundary Consideration

The above modelling of the plate assumes simply support boundaries at four edges. In the application of tension-aligned array structures, the array panels are usually connected through tensioners to the support structures. In such a scenario, boundaries of plates which are used to model the array panels are no longer fixed to ground. The edges are suspended by tensions and they acquire some flexibility, as shown in Fig. 25 and 26. This more realistic boundary condition was investigated regarding if it compromises the control idea that is based on varying tension which operates on suspended boundaries.

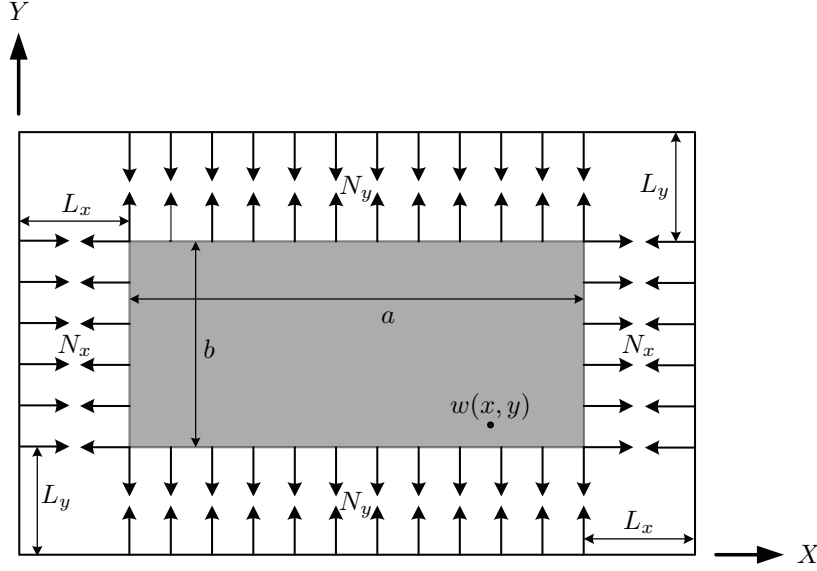


Figure 25: Plate subject to tension with tension suspension boundary conditions

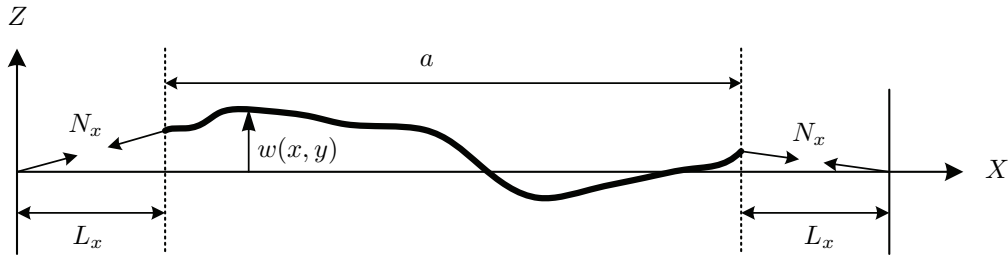


Figure 26: Side view of a plate with tension suspension boundary conditions

As shown in Fig. 25 and 26, consider normal in-plane tensions N_x and N_y . They connect the edges of the plate to the support structure which can be treated as fixed. There are distances between the plate edges and the support from which the tensions are imparted. Assume these distances are L_x and L_y , symmetric in opposite sides. Since the plate edges are suspended, they are allowed to rotate and have transverse displacements. Directions of the tensions are not always parallel to the X-Y plane. They change accordingly as the edges translate. This configuration

changes the stiffness of the system in a way that more terms are added into the stiffness since additional strain energy is created due to the tensions as the edges move transversely. The tension-induced stiffness terms K_x and K_y in Eq. (76) need to be reformulated as

$$K_x = \int \int \frac{\partial \phi_i}{\partial x} \frac{\partial \phi_j}{\partial x} dx dy + \underbrace{\frac{1}{L_x} \int_0^b [\phi_i(0, y) \phi_j(0, y) + \phi_i(a, y) \phi_j(a, y)] dy}_{\text{additional terms}} \quad (86)$$

$$K_y = \int \int \frac{\partial \phi_i}{\partial y} \frac{\partial \phi_j}{\partial y} dx dy + \underbrace{\frac{1}{L_y} \int_0^a [\phi_i(x, 0) \phi_j(x, 0) + \phi_i(x, b) \phi_j(x, b)] dx}_{\text{additional terms}} \quad (87)$$

where in Eqs. (86) and (87), line integrations are performed to account for the contribution of the transverse displacements of the edges made into the strain energy and into the system stiffness.

With the formulation of Eqs. (86) and (87) presented, basis functions that assume the displacement shape of the plate also need to be modified. Sine functions used before in Rayleigh-Ritz method are no longer suited since geometry boundary conditions allow the edges to move. In this case, a finite element model is well-suited since it is capable of describing large range of geometry and boundary conditions. Rayleigh-Ritz method is still an option for the modelling, but the basis functions need to be changed to a more complicated form. In [36] a set of functions combining sinusoidal series and fourth-order polynomials are provided. No matter which discretization method is employed, the system stiffness keeps the same form as Eq. (76). This indicates changing the boundary conditions from simply supported into tension suspended does not affect the control strategy. To verify this, simulation was done using the same plate geometry and properties as shown in Table 4. Distances between the edges and the fixed support are taken as $L_x = L_y = 0.1$ m. Initial condition was created by setting at $t = 0$

$$X_p = [1.00 \ 0.30 \ 0.20 \ 0.10 \ 0.05 \ 0.04]^T \times 10^{-2}$$

and $\dot{X}_p = 0$. Simulation results are shown in Fig. 27.

Results in Fig. 27 compares the results between direct control application (no filter) and free vibration (no control) cases. In Fig. 27 (a), no control was applied and Lyapunov energy defined in Eq. (80) was dissipated only through internal material damping. At $t = 40$ s, there was 63% of the starting vibration energy remained in the plate. While as shown in Fig. 27 (b), remaining energy was negligible in the system and vibration was completely suppressed by this control strategy. Displacement plots sampled at one point on the plate are also shown in 27 (c) and (d). The comparison demonstrates the efficacy of the control strategy based on tension varying is retained under the more realistic boundary conditions.

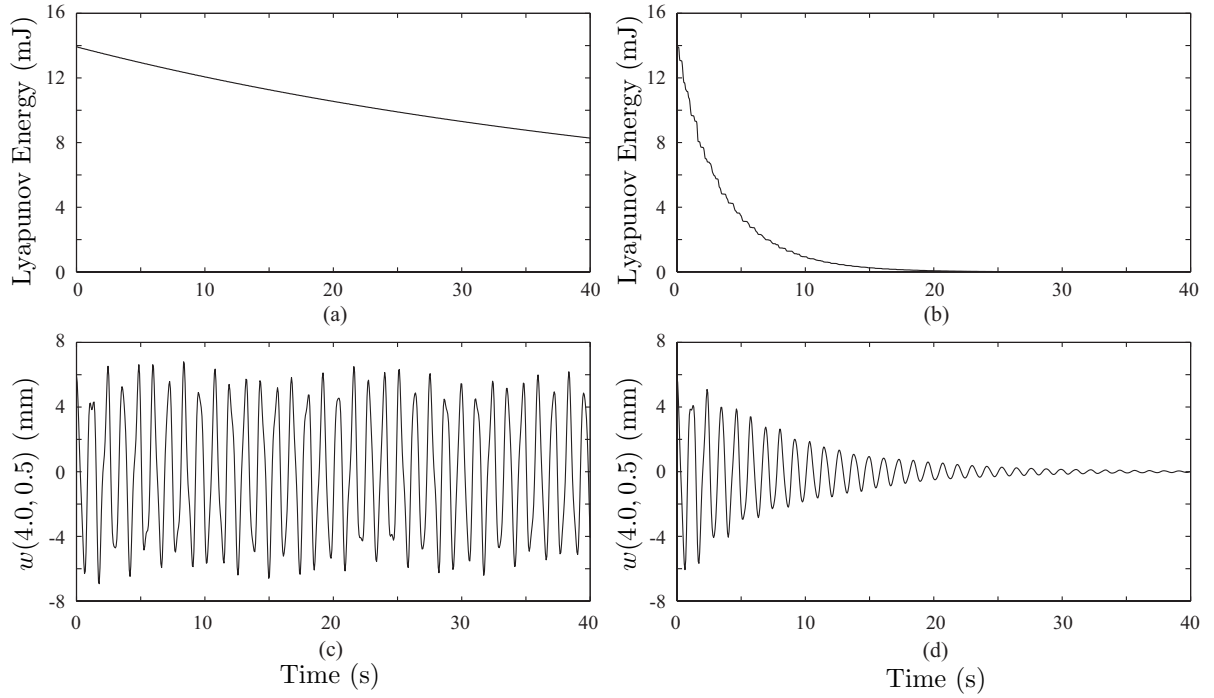


Figure 27: Simulation of control results of a plate with tension suspension boundary conditions: (a)(b) Lyapunov energy of the uncontrolled and controlled systems; (c)(d) Transverse displacement of the uncontrolled and controlled systems, sampled at $(x = 4.0, y = 0.5)$

5 Additional Work

In the last three sections, the antenna was modeled as a plate or a beam, *i.e.*, as a structural element with bending stiffness. Since a lot of attention has been given to gossamer structural elements such as membranes, we conducted separate studies on vibration suppression in strings and membranes. Some of these studies have already been published; the publications are listed on the second page of this report.

References

- [1] Mikulas, M., Murphey, T. and Jones, T. C., 2008, “Tension-Aligned Deployable Structures for Large 1-D and 2-D Array Applications”, *49th AIAA Structures, Structural Dynamics, and Materials Conference*, Schaumburg, IL.
- [2] Jones, T. C., Waston, J. J., Mikulas, M. and Bart-Smith, H., 2008, “Design and Analysis of Tension-Aligned Large Aperture Sensorcraft”, *49th AIAA Structures, Structural Dynamics, and Materials Conference*, Schaumburg, IL.
- [3] Adler, A., Mikulas, M. M., Hedgepeth, J. M., Stallard, M. and Garnham, J., 1998, “Novel Phased Array Antenna Structure Design”, *IEEE Aerospace Conference*, Aspen, CO.

- [4] Winslow, C., 1993 “Space Station Freedom Solar Array Design Development”, *IEEE Aerospace and Electronic Systems Magazine*, **8**(1), pp. 3-8.
- [5] Fang, J. and Lyons, G. J., 1996, “Structural Damping of tensioned Pipes with Reference to Cables”, *Journal of Sound and Vibration*, **194**(3), pp.891-907.
- [6] Kemerley, R. T. and Kiss, S., 2000 “Advanced Technology for Future Space-Based Antennas”, *IEEE MTT-S International Microwave Symposium Digest*, Boston, MA, pp.717-720.
- [7] Jeon, S. K. and Murphey, T. W, 2012 “Fundamental Design of Tensioned Precision Deployable Space Structures Applied to an X-Band Phased Array”, *53rd AIAA Structures, Structural Dynamics, and Materials Conference*, Honolulu, HI.
- [8] Footdale, J. N., Jeon, S. K. and Murphey, T. W, 2012 “Static Shape and Modal Testign of a Deployable Tensioned Phased Array Antenna”, *53rd AIAA Structures, Structural Dynamics, and Materials Conference*, Honolulu, HI.
- [9] Jones, T. C., Bart-Smith, H., Mikulas, M. and Watson, J. 2007, “Finite Element Modeling and Analysis of Large Pretensioned Space Structures”, *Journal of Spacecraft and Rockets*, **4**(1), pp.183-193.
- [10] Onoda, J., Endo, T., Tamaoki, H. and Watanabe, N., 1991, “Vibration Suppression by Variable-Stiffness Members”, *AIAA Journal*, **29**(6), pp.977-983.
- [11] Onoda, J., Sano, T. and Kamiyama, K., 1992, “Active, Passive, and Semiactive Vibration Suppression by Stiffness Variation”, *AIAA Journal*, **30**(12), pp.2922-2929.
- [12] Clark, W. W., 2000, “Vibration Control with State-Switching Piezoelectric Materials”, *Journal of Intelligent Material Systems and Structures*, **11**(4), pp.263-271.
- [13] Corr, L. R. and Clark, W. W., 2001, “Energy Dissipation Analysis of Piezoceramic Semiactive Vibration Control”, *Journal of Intelligent Material Systems and Structures*, **12**(11), pp.729-736.
- [14] Ramaratnam, A. and Jalili, N., 2006, “A Switched Stiffness Approach for Structural Vibration Control: Theory and Real-Time Implementation”, *Journal of Sound and Vibration*, **291**(1-2), pp.258-274.
- [15] Diaz, A. R. and Mukherjee, R., 2006, “Topology Optimization Problem in Control of Structures using Modal Disparity”, *ASME Journal of Mechanical Design*, **128**(3), pp.536-541.
- [16] Diaz, A. R. and Mukherjee, R., 2008, “Optimal Joint Placement and Modal Disparity in Control of Flexible Structures”, *Computers and Structures*, **86**(13-14), pp. 1456-1462.
- [17] Issa, J., Mukherjee, R. and Diaz, A. R., 2009, “Energy Dissipation in Dynamical Systems Through Sequential Application and Removal of Constraints”, *ASME Journal of Dynamic Systems, Measurement and Control*, **131**(2).
- [18] Barhorst. A. A., 2004, “On the Efficacy of Pseudo-Coordinates. Part 1: Moving Interior Constraints”, *International Journal of Non-Linear Mechanics*, **39**(1), pp. 123-135.
- [19] Hong, D. and Ren. G., 2011, “A Modeling of Sliding Joint on One-Dimensional Flexible Medium”, *Multibody System Dynamics*, **26**(1), pp. 91-106.

- [20] Sakamoto. H. and Park, K, C, 2006, “Localized Vibration Isolation Strategy for Low-Frequency Excitations in Membrane Space Structures’, *Journal of Vibration and Acoustics: Transactions of the ASME*, **128**(6), pp. 790-797.
- [21] Diaz, A. R. and Mukherjee, R., 2006, “Modal Disparity Enhancement through Optimal insertion of Nonstructural Masses”, *Structural and Multidisciplinary Optimization*, **31**(1), pp.1-7.
- [22] Issa, J., Mukherjee, R., Diaz, A. R. and Shaw, S. W., 2008, “Modal Disparity and its Experimental Verification”, *Journal of Sound and Vibration*, **311**(3-5), pp.1465-1475.
- [23] Perkins, N. C., 1990, “Planar Vibration of an Elastica Arch - Theory and Experiment”, *ASME Journal of Vibration and Acoustics* **112**(3), pp.374-379.
- [24] Dill, E. H., 1992, “Kirchhoff’s Theory of Rods”, *Archive for History of Exact Sciences*, **44**(1), pp.1-23.
- [25] Love, A. E. H., 1944, *A Treatise on the Mathematical Theory of Elasticity*, Dover, NY.
- [26] Perkins, N. C. and Mote, C. D., Jr., 1987, “Three Dimensional Vibration of a Translating Elastic Cable”, *Journal of Sound and Vibration*, **114**(2), pp. 325-340.
- [27] Rao, S. S, 2007, *Vibration of Continuous Systems*, Wiley, NJ.
- [28] Popov, V. L., 2010, *Contact Mechanics and Friction: Physical Principles and Applications*, Springer, NY.
- [29] Fischer-Cripps, A. C., 2007, *Introduction to Contact Mechanics*, Springer, NY.
- [30] Bauchau, O. A., 2010, *Flexible Multibody Dynamics*, Springer, NY.
- [31] Wittbrodt, E., 2006, *Dynamics of Flexible Multibody Systems: Rigid Finite Element Method* Springer, Berlin.
- [32] Spencer, A. J. M., 1980, *Continuum Mechanics*, Longman Group Limited, London.
- [33] Nudehi, S., Mukherjee, R. and Shaw S. W., 1992, “Active Vibration Control of a Flexible Beam Using a Buckling-Type End Force”, *ASME Journal of Dynamic Systems Measurement and Control*, **128**(2), pp. 278-286.
- [34] Issa, J., Mukherjee, R. and Shaw S. W., 1992, “Vibration Suppression in Structures Using Cable Actuators”, *ASME Journal of Dynamic Systems Measurement and Control*, **132**(3).
- [35] Khalil, H., 2002, *Nonlinear Systems*, Prentice Hall, NJ.
- [36] Li, W. L., 2003, “Vibration Analysis of Rectangular Plates with General Elastic Boundary Supports”, *Journal of Sound and Vibration*, **273**(3), pp. 619-635